AA Technical Memorandum ERL ARL-123

A STUDY OF THE PROBABLE ENVIRONMENTAL IMPACT OF FUGITIVE COAL DUST EMISSIONS AT THE RAVENSWOOD POWER PLANT, NEW YORK

Air Resources Laboratory
Rockville, Maryland
July 1983

noaa NATIONAL OCEANIC AND ATMOSPHERIC ADMINISTRATION / Environmental Research Laboratories

NOAA Technical Memorandum ERL ARL-123

A STUDY OF THE PROBABLE ENVIRONMENTAL IMPACT OF FUGITIVE COAL DUST EMISSIONS AT THE RAVENSWOOD POWER PLANT, NEW YORK

K. Shankar Rao

Atmospheric Turbulence and Diffusion Division
Oak Ridge, Tennessee

Lynne Satterfield

Oak Ridge Associated Universities
Oak Ridge, Tennessee

Air Resources Laboratory
Rockville, Maryland
July 1983

UNITED STATES
DEPARTMENT OF COMMERCE

Malcolm Baldrige,
Secretary

NATIONAL OCEANIC AND
ATMOSPHERIC ADMINISTRATION

John V. Byrne,
Administrator

Environmental Research
Laboratories

Vernon E. Derr
Acting Director

NOTICE

Mention of a commerical company or product does not constitute an endorsement by NOAA Environmental Research Laboratories. Use for publicity or advertising purposes of information from this publication concerning proprietary products or the tests of such products is not authorized.

ATDL Contribution File No. 83/11

CONTENTS

	page
TABLES	iv
FIGURES	v
ACKNOWLEDGEMENTS	ix
ABSTRACT	x
1. INTRODUCTION	1
2. NATURE OF THE PROBLEM	3
3. MODEL FORMULATION	5
4. EMISSION AND DRIFT CHARACTERIZATION	10
4.1 Lognormal Distribution	10
4.2 Drift Mass Distribution	13
4.3 Gravitational Settling and Deposition Velocities	13
5. SITE METEOROLOGY	16
6. MODEL PARAMETERS AND CALCULATIONS	18
6.1 Model Parameters	18
6.2 Calculation Procedure	20
7. RESULTS AND DISCUSSION	23
7.1 Ground-level Concentrations	23
7.2 Atmospheric Concentration and Visibility Profiles	24
7.3 Hourly Deposition Fluxes	26
7.4 Monthly Deposition Fluxes	27
7.5 Yearly Deposition Fluxes	30
7.6 Net Deposition Rates	31
8. CONCLUSIONS AND RECOMMENDATIONS	34
REFERENCES	40

TABLES

Number		Page
1	Coal drift mass distribution	42
2	Drift characteristics	42
3	Wind speed classification	42
4	Monthly joint frequencies of wind speed and wind direction for the month of January, 1974-78 (Case I)	43
5	Yearly joint frequencies of wind speed and wind direction for the years 1974-78 (Case I)	44
6	Monthly joint frequencies of wind speed and wind direction for the month of January, 1974-78 (Case II)	45
7	Yearly joint frequencies of wind speed and wind direction for the years 1974-78 (Case II)	46
8	Values of coefficients in Briggs' (1973) formulas for $\sigma_y(x)$ and $\sigma_z(x)$ in urban conditions	47
9	Seasonal stratification of months	47
10	Net deposition rate (kg/month) for January (Case I)	48
11	Net deposition rate (kg/month) for January (Case II)	50
12	Yearly net deposition rate (Case I)	52
13	Yearly net deposition rate (Case II)	54

FIGURES

Number		Page
1	Stationary coal unloading tower	56
2	Lognormal probability plot of particle size distributions by number (line A) and by weight (line B) for Wyoming coal	57
3	Variation of ground-level centerline concentration with downwind distance, shown as a function of wind speed, for Case I	58
4	Variation of ground-level centerline concentration with downwind distance, shown as a function of wind speed, for Case II	59
5	Vertical profiles of atmospheric concentration and visibility at several downwind distances (Case I)	60
6	Vertical profiles of atmospheric concentration and visibility at several downwind distances (Case II)	61
7	Variation of sector-average hourly surface deposition flux with downwind distance, shown as a function of wind speed, for Case I	62
8	Variation of sector-average hourly surface deposition flux with downwind distance, shown as a function of wind speed, for Case II	63
9	Isopleths of sector-average monthly surface deposition flux (kg/km^2/month) in the near-field region for the month of January (Case I)	64
10	Isopleths of sector-average monthly surface deposition flux (kg/km^2/month) in the far-field region for the month of January (Case I)	65
11	Isopleths of sector-average monthly surface deposition flux (kg/km^2/month) in the near-field region for the month of April (Case I)	66
12	Isopleths of sector-average monthly surface deposition flux (kg/km^2/month) in the far-field region for the month of April (Case I)	67

FIGURES (continued)

Number		Page
13	Isopleths of sector-average monthly surface deposition flux (kg/km^2/month) in the near-field region for the month of July (Case I)	68
14	Isopleths of sector-average monthly surface deposition flux (kg/km^2/month) in the far-field region for the month of July (Case I)	69
15	Isopleths of sector-average monthly surface deposition flux (kg/km^2/month) in the near-field region for the month of October (Case I)	70
16	Isopleths of sector-average monthly surface deposition flux (kg/km^2/month) in the far-field region for the month of October (Case I)	71
17	Isopleths of sector-average monthly surface deposition flux (kg/km^2/month) in the near-field region for the month of January (Case II)	72
18	Isopleths of sector-average monthly surface deposition flux (kg/km^2/month) in the far-field region for the month of January (Case II)	73
19	Isopleths of sector-average monthly surface deposition flux (kg/km^2/month) in the near-field region for the month of April (Case II)	74
20	Isopleths of sector-average monthly surface deposition flux (kg/km^2/month) in the far-field region for the month of April (Case II)	75
21	Isopleths of sector-average monthly surface deposition flux (kg/km^2/month) in the near-field region for the month of July (Case II)	76
22	Isopleths of sector-average monthly surface deposition flux (kg/km^2/month) in the far-field region for the month of July (Case II)	77
23	Isopleths of sector-average monthly surface deposition flux (kg/km^2/month) in the near-field region for the month of October (Case II)	78
24	Isopleths of sector-average monthly surface deposition flux (kg/km^2/month) in the far-field region for the month of October (Case II)	79

FIGURES (continued)

Number		Page
25	Isopleths of sector-average yearly surface deposition flux (kg/km^2/year) in the near-field region (Case I)	80
26	Isopleths of sector-average yearly surface deposition flux (kg/km^2/year) in the far-field region (Case I)	81
27	Isopleths of sector-average yearly surface deposition flux (kg/km^2/year) in the near-field region (Case II)	82
28	Isopleths of sector-average yearly surface deposition flux (kg/km^2/year) in the far-field region (Case II)	83

ACKNOWLEDGEMENTS

This report was prepared for the Oak Ridge National Laboratory (ORNL) as input to environmental impact statement work performed by ORNL in relation to the ERA-Fuel Use Act program. This work was accomplished under interagency agreements among the Atmospheric Turbulence and Diffusion Division (ATDD) of the National Oceanic and Atmospheric Administration (NOAA), the U. S. Department of Energy, and ORNL. The authors wish to thank the ORNL's project officers, Mr. Frank Kornegay and Mr. Norman Hinkle, for their interest and cooperation, and for supplying the meteorological and other data used in this work. The authors gratefully acknowledge the help of their colleague, Mr. Walter Culkowski, of the ATDD staff for supplying the coal handling, sizing, and source information. Special thanks are due to Dr. Ray Hosker of ATDD for useful suggestions and discussions during the course of this work, and Dr. Jack Shreffler of Environmental Sciences Research Laboratory of the U. S. Environmental Protection Agency for reviewing the draft report and suggesting improvements. Mrs. Mary Rogers of Oak Ridge Associated Universities (ORAU) provided able and patient typing assistance.

ABSTRACT

The Ravenswood Power Plant of the Consolidated Edison Company of New York is being converted to use coal as the primary fuel. This report addresses the probable short and long-term air pollution impacts of the fugitive coal dust emissions that are likely to occur during the coal unloading at the facility.

The coal drift consists of particles ranging in size from 0.1 to 200 μm. Assuming a lognormal probability of the particle size distribution, a drift mass spectrum was developed for six particle size ranges considered in the study. A steady state atmospheric advection-diffusion model that accounts for the gravitational settling and dry deposition of the particles was formulated, and an analytical solution, consistent with the basic assumptions of the Gaussian plume model, was derived and applied to the present study. The meteorological data used consist of a five year record of hourly surface wind observations. Six wind speed classes and sixteen wind direction classes were considered in the analyses.

This study considers two different coal unloading schedules: coal is unloaded only during daytime (0700-1900 hrs.) in Case I, and around the clock (both day and night) in Case II. The calculated results of ground-level concentrations, atmospheric concentrations and visibilities, hourly surface deposition fluxes, and deposition flux and net deposition rates on monthly and yearly basis were presented for Cases I and II separately.

1. INTRODUCTION

The Ravenswood Power Plant of the Consolidated Edison Company of New York is located on the east side of the East River, opposite 70th St. in Manhattan. It is presently being converted to use coal as the primary fuel. The coal will be delivered to the plant in large 5 m draft barges down the East River. The barge capacities range from 2000 tons to a proposed 6000 tons of coal.

There is no provision for ground storage of coal at Ravenswood and coal has to be handled directly from the barges. A unique feature of this system is a new stationary coal unloading tower (Carey *et al.*, 1967), shown in Fig. 1, consisting of a mobile clam-shell with a maximum travel of 27 m. The coal barges will be manipulated into position near the tower for unloading, and the coal is scooped up by the clam-shell and dumped into a 250 ton capacity bottom hopper that feeds the raw coal conveying system. The latter consists of a series of belt conveyors delivering coal to the bunkers in the boiler house.

The coal unloading tower is equipped with a dust control system and blowers for pressurizing the operator's cab and machinery room. The belt conveyors are mostly enclosed; where they are exposed to the weather, specially formed covers are installed to prevent snow and rain from accumulating on the coal in transit. Flap gates are installed for these sections for dust dispersal prevention.

The plant design incorporates an elaborate system for fly ash, bottom ash, and pyrites handling, a covered hot ash storage silo, wet scrubbers, and a high-temperature precipitator. These systems substantially reduce the fly ash emissions from the plant.

Almost all of the fugitive dust emissions from the plant are, therefore, likely to occur during the coal unloading from the barges. The stationary coal tower, equipped with a 17-ton coal bucket, has a maximum free digging capacity of 1800 tons/hr and is guaranteed to unload a 2300 ton coal barge in 110 min. Due to these large coal handling rates, more or less on a continuous basis while the plant is operating at full load, the likely fugitive coal dust emissions from the Ravenswood facility are significant enough to warrant a detailed environmental impact study.

This report addresses the probable short- and long-term air pollution impacts of the fugitive coal dust emissions from the Ravenswood conversion to coal.

2. NATURE OF THE PROBLEM

Breakage of coal occurs during its mining and subsequent handling due to its brittleness. All fuel coals, irrespective of their origin, contain some fines. While unloading the coal from the barges and transferring it to the hopper, some of these coal fines escape into the atmosphere as drift. The drift emission rate is usually only a small fraction of the coal unloading rate, and can be substantially reduced by coal washing and using spill plates, screens, and other devices as drift eliminators.

The coal drift consists of various particle sizes ranging from 0.1 to 200 μm. The larger particles, due to their weight, fall off to the ground in the immediate vicinity of the coal unloading tower. The medium and smaller particles become airborne, dispersed by turbulence, and eventually deposited on the ground. The smaller the particle, the longer is its residence time in the atmosphere. Most of the deposition occurs within 10 km from the plant.

The surface deposition flux depends on the gravitational settling and deposition velocities, which are primarily functions of the particle size. The drift mass distribution over the various particle size ranges, therefore, influences the pollutant mass concentration in the atmosphere and the surface deposition flux at a given downwind location.

Smaller particles, due to their larger travel distances and longer residence times in the atmosphere, have an adverse impact on human health and visibility. Particles smaller than 6 μm can escape the defense mechanisms of the upper respiratory system and enter the lung. Particles in two size ranges, namely, with diameters of about 0.1 μm and

1 μm are most effectively retained in the lung (Williamson, 1973). Light scattering by particles is the dominant cause of reduced visibility through polluted air. Particles smaller than 10 μm size contribute to the degradation of visibility beyond the immediate vicinity of the plant.

For a given coal-drift emission rate, the atmospheric particulate concentration and surface deposition flux are primarily influenced by the mean wind speed and its direction, and the drift particle size and mass distribution. Though atmospheric stability also influences the turbulent diffusion and the resulting atmospheric concentrations of particles on a short-term basis, it is secondary to the above factors in its effect on the surface deposition flux calculated on a monthly or yearly basis. The mixing depth (or the height of the inversion lid) also influences the atmospheric dispersion beyond a certain distance downwind of the source. The model used in the study should account for these various factors.

The major components of this impact study are the following: 1) model formulation, 2) emission and drift characterization, 3) site meteorology, 4) calculated results including atmospheric concentrations and visibilities, ground level concentrations, surface deposition flux and net deposition rates on a monthly and yearly basis, and 5) conclusions and recommendations.

3. MODEL FORMULATION

We consider the steady state form of the atmospheric advection-diffusion equation:

$$U\,\partial C/\partial x = K_y\,\partial^2 C/\partial y^2 + K_z\,\partial^2 C/\partial z^2 + W\,\partial C/\partial z \tag{1}$$

Here x, y, z are the downwind, lateral, and vertical coordinates, respectively; U is the constant average wind speed, W is the gravitational settling velocity of the pollutant particle, C is the pollutant concentration at (x,y,z), and K_y and K_z are the eddy diffusivities in the lateral and vertical directions, assumed to be functions only of the downwind distance, x.

For a continuous point source of strength Q located at (0,0,h), the boundary conditions are given by

$$C(0,y,z) = Q/U \cdot \delta(y) \cdot \delta(z - h) \tag{2a}$$

$$C(\infty,y,z) = 0 \tag{2b}$$

$$C(x,\pm\infty,z) = 0 \tag{2c}$$

$$C(x,y,\infty) = 0 \tag{2d}$$

$$[K_z \cdot \partial C/\partial z + WC]_{z=0} = [V_d C]_{z=0} \tag{2e}$$

In the above, δ is the Dirac-Delta function such that $\int\delta(x)dx \equiv 1$ when $x = 0$, and $\delta(x) \equiv 0$ when $x \neq 0$; V_d is the deposition velocity which characterizes the interaction between the diffusing pollutant and the surface. For $V_d = 0$, the lower boundary acts as a perfect reflector for

pollutant particles; for $V_d = \infty$, it acts as a perfect sink; for the more general case of $0 < V_d < \infty$, the pollutant particles reaching the earth's surface are partially retained and the rest reflected by it into the atmosphere.

The above formulations for the atmospheric diffusion of particulate material are discussed by Calder (1961). For constant K_y and K_z (Fickian diffusion), the exact analytical solution of the problem was originally given by Monin (1959), and subsequently by Smith (1962), Scriven and Fisher (1975), Rao (1975), and Ermak (1977). These solutions due to the various authors, though basically the same, differ somewhat due to the different source conditions (instantaneous/continuous, line/point, elevated/ground-level), pollutant-species (for gases or small particles, $W \equiv 0$; for large particles, $V_d \equiv W$), and other assumptions used in their studies.

Here, assuming Fickian diffusion, we express the constant eddy diffusivities K_y and K_z in terms of the Gaussian plume parameters, $\sigma_y(x)$ and $\sigma_z(x)$, in order to utilize the vast amount of empirical data on these parameters available in the literature:

$$K_y = \sigma_y^2 \cdot U/2x \ , \quad K_z = \sigma_z^2 \cdot U/2x \tag{3}$$

where σ_y^2 and σ_z^2 are the mean square particle diffusion parameters. Strictly speaking, these relations are valid only for homogeneous stationary turbulence at large x when $\sigma \sim x^{1/2}$, which gives constant K from Eq. (3), consistent with the Fickian diffusion. For small x ($x < 100$ m, say) when $\sigma \sim x$, Eq. (3) gives $K \sim x$ which disagrees with the Fickian assumption. This, however, is not a serious limitation. For

$100 < x < 10^4$ m, available empirical data (see Gifford, 1976) on $\sigma_y(x)$ and $\sigma_z(x)$, when used with Eq. (3), give reasonably good estimates of the concentrations and deposition fluxes.

The exact analytical solution of (1), subject to the boundary conditions (2) and auxiliary relations (3), can be written as follows:

$$C(x,y,z) = \frac{Q}{2\pi\sigma_y\sigma_z U} \cdot \exp\left\{-\frac{1}{2}\left(\frac{y}{\sigma_y}\right)^2\right\}$$

$$\cdot \left[\exp\left\{\frac{-2W(z-h) - W^2\frac{x}{U}}{2\sigma_z^2\frac{U}{x}}\right\}\right.$$

$$\left. \cdot \left[\exp\left\{-\frac{1}{2}\left(\frac{z-h}{\sigma_z}\right)^2\right\} + \exp\left\{-\frac{1}{2}\left(\frac{z+h}{\sigma_z}\right)^2\right\}\right]\right.$$

$$- \sqrt{2\pi}\,\frac{(2V_d - W)}{U}\,\frac{x}{\sigma_z} \cdot \exp\left\{\frac{V_d h + (V_d - W)z + V_d(V_d - W)\frac{x}{U}}{\sigma_z^2\frac{U}{2x}}\right\}$$

$$\left. \cdot \operatorname{erfc}\left\{\frac{z + h + (2V_d - W)\frac{x}{U}}{\sqrt{2}\,\sigma_z}\right\}\right] \qquad (4)$$

This equation is physically and dimensionally correct and is consistent with the solutions given by Smith (1962) for a uniform crosswind line source and Rao (1975) for a continuous elevated point source. In the trivial deposition case of $V_d = 0$ and $W = 0$, Eq. (4) reduces to the well-known Gaussian plume model.

The ground-level plume centerline concentration, $C(x,0,0)$, can be obtained by setting $y = 0$ and $z = 0$ in Eq. (4). The sector-averaged

ground-level concentration in air over a 22.5° sector can then be calculated as

$$C_{SA}(x) = C(x,0,0) \cdot R \tag{5}$$

where $R = \sqrt{2\pi}\ \sigma_y/2x \tan 11.25° = 6.301\ \sigma_y/x$.

The sector-averaged deposition flux, D(x), can be calculated as

$$D(x) = C_{SA}(x) \cdot V_d \tag{6}$$

This is the amount of pollutant deposited per unit time per unit surface area. D is usually calculated as $kg/km^2/hr$, while seasonal estimates of D are expressed as $kg/km^2/month$. The estimation of the monthly or yearly surface deposition fluxes at a given downwind distance x from the source in a given wind-directional sector requires the knowledge of the fraction of the time that a mean wind of a given magnitude blows in that direction in a month or a year, respectively, on a climatological basis.

The net deposition rate, N(x), which is the total amount of pollutant deposited per unit time between the source and the downwind distance x, can be calculated from Eq. (6) as

$$N(x) = \int_0^x D(x') \cdot b(x') \cdot dx' \tag{7}$$

where $b(x') = 2x' \tan 11.25°$ is the width of the 22.5° sector at x'. The units of N(x) are kg/hr, while the seasonal estimates of N(x) are expressed as kg/month. It is often more useful to calculate the net deposition rate between two given downwind distances x_1 and x_2. From Eq. (7), this can be obtained as

$$N_{x_2-x_1} = \int_{x_1}^{x_2} D(x') \cdot b(x') \cdot dx' \tag{8a}$$

If the distance $x_2 - x_1$ is sufficiently small compared to the length scale, $D/(\partial D/\partial x)$, characterizing the variation of D, the integral in Eq. (8a) can be evaluated, to a good approximation, as

$$N_{x_2-x_1} = \frac{1}{2} [D(x_2) + D(x_1)] \cdot [A(x_2) - A(x_1)] \tag{8b}$$

where $A(x) = \pi x^2/16$ is the area of the 22.5° sector between the source and the downwind distance x. Thus, knowing $D(x_1)$ and $D(x_2)$, the net deposition rate between x_1 and x_2 can be estimated from Eq. (8b).

4. EMISSION AND DRIFT CHARACTERIZATION

The source strength Q in Eq. (4) represents the coal dust emission rate in g/s. This airborne drift is usually only a small fraction of the total coal unloading rate. The latter is about 1255 tons/hr at the Ravenswood plant, based on the guaranteed maximum unloading capacity of the coal bucket. In this study, the drift rate is taken as 0.01% of this coal unloading rate, based on our consultations with the manufacturers of the stationary coal tower. This gives a drift source strength Q = 31.63 g/s. The atmospheric concentration, surface deposition flux and net deposition rate, calculated as given in the previous section, are linearly proportional to the source strength. This implies that C/Q, D/Q, and N/Q are independent of Q. For values of Q significantly different from the one used in this study, therefore, C, D, and N can be obtained by simple multiplication of the present results by the appropriate source-scaling factor.

The drift consists of various particle sizes ranging from 0.1 to 200 μm. For purposes of this study, it is necessary to develop a spectrum of drift mass distribution among the various particle size ranges, since C, D, and N depend on the gravitational settling velocity (W) and deposition velocity (V_d) of the particle, which in turn depend on the drift particle size.

4.1 Lognormal Distribution

It is well known that number or weight versus size distributions of small particles resulting from both natural and mechanical processes follow the logarithmic form of the Gaussian statistical law of errors

(normal law). In the domain of small particle statistics, the lognormal distribution is well established. When the lognormal law is utilized, the statistical mean and deviation from the mean are changed from arithmetic to geometric averaging. This is explained below.

Let $d_1, d_2, \ldots, d_n$ be the particle sizes, and $t_1, t_2, \ldots, t_n$ be the corresponding transformed variables, where $t = \ell n\ d$. Then, if the probability density p of the distribution is given by

$$p = \frac{1}{\sqrt{2\pi}\ \sigma_t} \exp\left\{ - \frac{(t - \bar{t})^2}{2\sigma_t^2} \right\} \tag{9}$$

where $\bar{t}$ is the mean and σ_t is the standard deviation, then the particle sizes d_i are said to be lognormally distributed.

The mean $\bar{t}$ is given by

$$\bar{t} = \ell n\ d_g = \frac{1}{n} \sum_{i=1}^{n} \ell n\ d_i \tag{10a}$$

where

$$d_g = (d_1 \cdot d_2 \cdot \ldots d_n)^{1/n} \tag{10b}$$

is the geometric mean which has the same units as the particle size.

The standard deviation (s.d.) σ_t is given by

$$\sigma_t = \ell n\ \sigma_g \tag{11a}$$

where

$$\sigma_g = \frac{\text{particle size at 84.13\% probability}}{\text{particle size at 50\% probability}}$$

$$= \frac{\text{particle size at 50\% probability}}{\text{particle size at 15.87\% probability}} \tag{11b}$$

is the geometric s.d., which is the s.d. of the distribution of ratios of particle sizes around the geometric mean. Thus, the lognormal distribution suggests that ratios of equal amount in excess or deficit from a mean value are equally likely. It should be noted that the geometric s.d., σ_g, is a dimensionless ratio, whereas the arithmetic s.d. has the same units as the arithmetic mean. These two parameters of the lognormal law, namely d_g and σ_g, often evaluated graphically, adequately describe the size distributions of the particulate matter.

In particle grading, the size distribution is usually measured by number or weight, but determined by a linear test such as sieving or microscopic measurement. Hatch (1933) and Herdan (1960), among others, have shown that if the particle size distribution gives a straight line on a number basis, when plotted on log-probability graph paper, the size distribution by weight (volume) or surface area is a parallel straight line on the same coordinates. Thus, both the weight and number distributions are lognormal with the same log standard deviation, σ_t.

Figure 2 shows the number and weight lognormal distributions by straight lines A and B, respectively, for the low-sulfur Wyoming coal expected to be used by the Ravenswood plant. The lognormal particle number distribution (line A), with a geometric mean of 4.5 μm and a s.d. of 4.29, was provided by the Fossil Fuel Analysis Division of the Oak Ridge National Laboratory (ORNL). From this, the lognormal weight distribution (line B) was constructed by using Kapteyn's law (Herdan, 1960) which can be stated as follows: If the basic (number) distribution is lognormal with mean $\bar{t}_o$ and s.d. σ_t, then the jth moment distribution is lognormal with the same s.d. σ_t, and a mean given by

$$\bar{t}_j = \bar{t}_o + j\,\sigma_t^2 \qquad (12)$$

Substituting $\bar{t}_o$ = ℓn 4.5, σ_t = ℓn 4.29, and j = 3 for weight (or volume) distribution, we obtain the geometric mean particle size of weight distribution as 2608 μm. Using this value for the mean, and σ_g = 4.29, line B can be then constructed. It should be noted that, according to line B, the 15.87% probability size corresponds to 608 μm.

4.2 Drift Mass Distribution

Figure 2, line B, indicates that the airborne drift mass, consisting of particles with $d_i \leq 200$ μm, constitutes 3.8% of the total mass; particles with $d_i \leq 100$ μm contain 1.25% of the total mass. Thus, 2.55% of the total mass or 67.11% of the drift mass is contained by particles in the 100-200 μm size range, with a representative diameter of 150 μm. Following this procedure, a complete drift mass distribution, shown in Table 1, can be computed from the lognormal size distribution by weight. Table 1 shows that particles less than 10 μm in size consist less than .3% of the total drift mass. However, due to the large value of the estimated fugitive emissions rate, the atmospheric concentrations of these fine, inhalable particles are expected to be significant. These small particles are important for health and visibility considerations, due to their longer residence times and larger travel distances in the atmosphere.

4.3 Gravitational Settling and Deposition Velocities

The drift mass spectrum shown in Table 1 has 6 particle-size ranges, each assigned with a drift mass fraction f_i and a representative diameter d_i. In order to use Eq. (4), it is necessary to assign values for the gravitational settling velocity (W) and the deposition velocity (V_d) for each particle size d_i.

For a monodisperse particulate cloud, the individual particles have a constant gravitational settling velocity. This terminal velocity is given by Stokes' equation (Fuchs, 1964):

$$W = \frac{d^2 \, g \, \rho}{18 \, \mu} \tag{13}$$

where d is the diameter of the particle, g is acceleration due to gravity, ρ is density of particles, and μ is the dynamic viscosity of air. For $d > 100$ μm, the terminal fall velocity is sufficiently great that turbulence in the wake of the particle cannot be neglected, and the viscous drag force on the particle is greater than given by the Stokes' law, $F_d = 3\pi d\mu W$; for a particle with $d = 400$ μm, the actual value of W is about one-third the value given by Eq. (13). Stokes' expression for the drag force describes the effects of collisions between air molecules and a particle assuming that air behaves as a fluid. This assumption is not valid for very small particles, since the mean free path between molecular collisions is comparable to the particle size. Under these conditions, "slippage" occurs, and the particles undergo Brownian motion and diffusion, which give a terminal velocity greater than that predicted by Eq. (13). A discussion of the slip correction factor for the Stokes' equation can be found in Fuchs (1964) and Cadle (1975).

The values for the terminal gravitational settling velocities for different particulate materials are given in a tabular from by Lapple (1961) based on particle diameter and Reynolds number. These values, which account for the deviations from Stokes' equation discussed above, are given for spherical particles with a specific gravity of 2.0 in air at 25°C and 1 atm. pressure. The settling velocities used in the present study are taken from this table.

The dry deposition pollutant-removal mechanisms at the earth's surface include gravitational settling, turbulent and Brownian diffusion, chemical absorption, inertial impaction, thermal, and electrical effects. Some of the deposited particles may be re-released into the atmosphere by mechanical resuspension. Following the concept introduced by Chamberlain (1953), particle removal rates from a polluted atmosphere to the surface are usually described by dry deposition velocities which vary with particle size, surface properties (including surface roughness (z_o) and moisture), and meteorological conditions. The latter include wind speed and direction, friction velocity (u_*), and thermal stratification of the atmosphere. Deposition velocities for a wide variety of substances and surface and atmospheric conditions may be obtained directly from the literature (e.g., McMahon and Denison, 1979; Sehmel, 1980). Sehmel and Hodgson (1974) gave plots relating deposition velocity (V_d) to d, z_o, u_*, and the Monin-Obukhov stability length. The values of V_d used in this study are adopted from their results.

For very small particles ($d < 0.1$ μm), gravitational settling can be neglected, and dry deposition occurs primarily due to the nongravitational effects mentioned above. For small particles ($d = 0.1$-20 μm), $0 < W < V_d$; for $d \geq 20$ μm, it is generally assumed $V_d = W > 0$, since gravitational settling is the dominant deposition mechanism. Reentrainment of dust particles ($W > V_d > 0$) was not considered here. The values of W and V_d used for the particle sizes considered in this study are shown in Table 2.

5. SITE METEOROLOGY

Meteorological data used in this study consist of the five-year record of surface observations taken at the LaGuardia Airport National Weather Service (NWS) Station during the period from 1 January, 1974 through 31 December, 1978. This NWS station is the nearest one to the Ravenswood plant. The chief advantage of using the surface data from this NWS station lies in the availability of long records of continuous hourly measurements required for this study.

The hourly averaged wind speed and direction data over the five year period were analyzed to determine the frequency of occurrence of a given wind speed in a given direction. Sixteen wind direction classes were considered based on the standard 16-point compass starting from 1 = N, 2 = NNE, ... , 16 = NNW, each direction representing the median of a 22.5° sector. Wind blowing from any angle in a given sector is assigned the number of that wind direction class.

Six wind speed classes were considered as shown in Table 3. Any wind speed which lies in a given range is assigned the number of that wind speed class. Using the hourly surface meteorological data over the five year period, tables of joint frequencies of occurrence of each category of wind direction in each class of wind speed were generated on a monthly and yearly basis.

Two different cases were considered in the meteorological as well as environmental impact analyses:

Case I: Daytime (0700-1900 hours) coal unloading only. This implies that the pollutant source is operating for 13 out of 24 hours in a day, or a pollutant loading factor P = 0.542 used to multiply the deposition flux calculated on a monthly or yearly basis.

Case II: Around the clock (24 hours per day) coal unloading. The pollutant loading factor P = 1.

In the meteorological data analyses for Case I, hourly data from only 0700-1900 hours for each day were included, whereas for Case II, data for all hours were included in the analyses. Using the five year (1974-1978) data base, 13 tables (12 monthly and one yearly) of joint frequencies were generated for each case, each table consisting of 96 fractional joint frequencies (16 wind directions × 6 wind speeds) for all possible combinations of these two parameters; all 96 elements in each table add up to 1. All tables for each case were stored separately in a computer file for easy linkup with the deposition model. As examples, Table 4 shows the monthly joint frequencies for the month of January, and Table 5 shows the yearly joint frequencies, both for Case I. Similar results for Case II are shown in Tables 6 and 7, respectively.

6. MODEL PARAMETERS AND CALCULATIONS

The model parameters, other than those discussed above, are given in this section. The procedure for calculating the atmospheric and ground-level concentrations, surface deposition fluxes and net deposition rates is described here.

6.1 Model Parameters

As noted earlier, the dominant meteorological factors that influence monthly or yearly deposition fluxes of particulate pollutants are the mean wind speed and direction. The atmospheric stability effects on turbulent diffusion are secondary in importance. Therefore, the meteorological data were not analyzed for atmospheric stability classification. Instead, the climatological-average stability class for the daytime (Case I) dispersion in the urban atmosphere was taken as Class B (moderately unstable); for the 24-hour dispersion case (Case II), the average stability class was taken as D (neutral). The corresponding climatological-average mixing depths for these two cases were taken as 1000 m and 500 m, respectively. These values are consistent with the mixing depth climatology of coastal New York, based on the work of Holzworth (1972).

The turbulent dispersion parameters, $\sigma_y(x)$ and $\sigma_z(x)$ in Eq. (4), used in this study follow Briggs' (1973) formulations for diffusion in urban conditions (see also, Gifford, 1976). These interpolation formulas agree with the Pasquill-Gifford (PG) σ curves in the range $10^2 < x < 10^4$ m, except that the formulas for σ_z for A and B stability conditions approximate the curves recommended by Smith (1968) for $\sigma_z > 100$ m. Briggs'

recommendations apply up to x = 10 km and may perhaps be extended to 20 km. These formulas were written in a convenient form for programming as follows:

$$\sigma_y(x) = \frac{a_y\, x}{(1 + .0004\, x)^{1/2}} \tag{14a}$$

$$\sigma_z(x) = \frac{a_z\, x}{(1 + b_z\, x)^{1/2}} \cdot (1 + c_z\, x) \tag{14b}$$

In the above equations, x is given in meters. The coefficients a_y, a_z, b_z, and c_z are functions of the stability class, and their values are given in Table 8. These values represent the enhanced diffusion over cities, compared with that over open country, due to the increased mechanical and thermal turbulence resulting from the increased surface roughness and the great heat capacity of the cities.

Following Turner (1970), it was assumed that σ_z increases with x to a maximum value of 0.47 L, where L is the mixing depth simulated by an inversion lid at z = L. When σ_z = 0.47 L, the upper boundary of the pollutant cloud reaches the inversion lid, and the latter limits its vertical spread. Therefore, after σ_z = 0.47 L was reached at $x = x_L$, σ_z was kept constant at that value for $x > x_L$. This treatment closely approximates the equation suggested for plume trapping conditions by Gifford (1968).

The source height, h, in Eq. (4) was taken in this study as 25 m. This is the average height of travel of the mobile clam-shell on the stationary coal unloading tower. This source height, though approximate, is fairly small, and does not affect the concentration values beyond a few tens of meters downwind of the source.

Though the actual coal unloading from the barges may be done intermittently or periodically through the day, it was assumed for the purpose of this study that coal will be unloaded continuously through the day at Ravenswood Plant at an average rate of 1255 tons/hr, of which 0.01% becomes airborne. This was expected to provide a conservative worst-case estimate of the pollutant concentrations and deposition fluxes due to the fugitive coal dust emission at Ravenswood.

6.2 Calculation Procedure

After specifying all the model parameters as discussed in the previous sections, the model calculations were performed for Case I and Case II separately. The calculation procedure was as follows:

a) An x distance grid was set up with 50 points from 0-20 km; the distance increments were 0.01 km from 0-0.1 km, 0.1 km from 0.1-2 km, 0.5 km from 2-4 km, and 1 km from 4-20 km. The values of $\sigma_y(x)$ and $\sigma_z(x)$ at these points as well as the areas A(x) of the corresponding 22.5° sector segments were computed and stored.

b) Equation (4) was applied to calculate the value of C/Q, at the given x and z coordinates for each of the six wind speeds (see Table 3). All calculations were performed at the plume centerline, i.e., $y \equiv 0$. The terms containing V_d or W in Eq. (4) were calculated separately so that they can be repeatedly computed over the six particle sizes (see Table 2) with different values for V_d or W. The total concentration (g/m^3) due to all particle sizes at the given (x, 0, z) for the given wind speed was then calculated as

$$C(x,0,z) = Q \cdot \sum_{i=1}^{6} \left(\frac{C}{Q}\right)_i \cdot f_i \qquad (15)$$

where the subscript i refers to the particle size class and f_i is its drift mass fraction, and Q is the total drift emission rate (g/s). The ground level concentrations C(x,0,0) were computed by setting z = 0 in Eq. (15).

c) Following Eqs. (5) and (6), and using the C/Q values for (x,0,0), the sector-average hourly surface deposition flux (kg/km^2/hr), D_H, due to all particle sizes at the given x and wind speed U_j was calculated and stored as

$$D_H(x,U_j) = 3.6 \times 10^6 \times R \times Q \cdot \sum_{i=1}^{6} \left(\frac{C}{Q}\right)_i \cdot f_i \cdot V_{di} \qquad (16)$$

where $R = 6.301\ \sigma_y(x)/x$.

d) Using the sector-average hourly deposition flux array, $D_H(x,U_j)$, and the monthly fractional joint-frequency array of wind speed and direction, $F_M(m,U_j,n)$, the monthly deposition flux (kg/km^2/month) array, D_M, was computed as

$$D_M(m,n,x) = 30 \times 24 \times P \cdot \sum_{j=1}^{6} D_H(x,U_j) \cdot F_M(m,U_j,n) \qquad (17)$$

In the above, m = 1, ... , 12 refers to the month, j = 1, ... , 6 refers to the wind speed, and n = 1, ... , 16 denotes the wind direction; P is pollutant loading factor (P = 0.542 for Case I and P = 1 for Case II).

e) Using the sector-average hourly deposition flux array, $D_H(x,U_j)$, and the yearly fractional joint-frequency array of wind speed and direction, $F_y(U_j,n)$, the yearly deposition flux (kg/km^2/year) array, D_y, was computed as

$$D_y(n,x) = 365 \times 24 \times P \cdot \sum_{j=1}^{6} D_H(x,U_j) \cdot F_y(U_j,n) \qquad (18)$$

f) Using the calculated monthly deposition flux array, $D_M(m,n,x)$, and following Eq. (8), the array of monthly net deposition rate (kg/month), N_M, between the successive x locations, x_i and x_{i+1}, was computed as

$$N_M(m,n,x_{i+1}) = \frac{1}{2}\,[D_M(x_{i+1}) + D_M(x_i)]_{m,n} \cdot [A(x_{i+1}) - A(x_i)] \qquad (19)$$

Similarly, the array of yearly net deposition rate (kg/year), N_y, was computed as

$$N_y(n,x_{i+1}) = \frac{1}{2}\,[D_y(x_{i+1}) + D_y(x_i)]_n \cdot [A(x_{i+1}) - A(x_i)] \qquad (20)$$

The percentage of the total emission rate of the pollutant deposited per month within a distance of 20 km from the plant was estimated as

$$P_m = \frac{\sum_{n=1}^{16} \sum_{i=1}^{50} N_M(m,n,x_i)}{Q \times 3.6 \times 24 \times 30 \times P} \times 100 \qquad (21)$$

The percentage of the total emission rate of the pollutant deposited per year within a distance of 20 km from the plant was estimated as

$$P_y = \frac{\sum_{n=1}^{16} \sum_{i=1}^{50} N_y(n,x_i)}{Q \times 3.6 \times 24 \times 365 \times P} \times 100 \qquad (22)$$

7. RESULTS AND DISCUSSION

The calculated concentration and deposition results for Cases I and II are presented and discussed in this section.

7.1 Ground-level Concentrations (GLC)

The ground-level centerline concentrations, C(x,0,0), for Case I are shown in Fig. 3 as functions of x and wind speed. The GLC increases as the wind speed decreases. At small x, the GLC increases with distance until it reaches a peak value. The magnitude and location of the peak GLC depend on the wind speed. For U = 1 m/s, a peak GLC of 0.1 g/m^3 occurs at x = 30 m; for U = 14 m/s, the peak value is 7.7×10^{-4} g/m^3 occurring at x = 70 m. For $0.1 < x < 1.3$ km, the decrease in GLC with distance is given by

$$C(x,0,0) \propto x^{-n} \tag{23}$$

where $n \cong 2$. This is represented by a straight line on the log-log plot shown in Fig. 3. This agrees with the vast amount of field diffusion data reported in literature (see Islitzer and Slade, 1968). At x = 1.3 km, the upper boundary of the pollutant cloud reaches the inversion lid at z = L = 1000 m. For x > 1.3 km, the GLC follows Eq. (23) with $n \cong 1.35$. In Fig. 3 (and several other figures in this report), the GLC (or the deposition fluxes) are plotted as the abscissae and x as the ordinate. This arrangement, while differing from conventional practice, proved convenient for computer-plotting of results, using available software, to suit the report format.

The ground-level centerline concentrations for Case II, plotted in Fig. 4, show similar variations, except that the values of GLC are larger in this case due to the smaller mixing depth (L = 500 m) and reduced turbulence. For U = 1 m/s, a peak GLC of 0.33 g/m^3 occurs at x = 32 m; for U = 14 m/s, the peak value is 9.5×10^{-4} g/m^3 occurring at x = 100 m. For 0.2 < x < 2 km, the GLC variation is given by Eq. (23) with n ≅ 2.0. At x ≅ 2 km, the upper boundary of the pollutant cloud reaches the inversion lid at z = L = 500 m. For x > 2 km, the GLC decreases less rapidly than without the influence of the inversion lid, and the GLC follows Eq. (23) with n ≅ 1.8.

7.2 Atmospheric Concentration and Visibility Profiles

The atmospheric concentration profiles of the pollutant, C(x,0,z), for Case I are shown in Fig. 5 at eight downwind locations for U = 4.5 m/s. The profiles for x = 0.03 km (Curve A) and 0.05 km (Curve B) show the elevated maxima of concentration, characteristic of the near-field diffusion from an elevated source. The large positive concentration gradients are indicative of the large deposition fluxes that occur in this region [see Eq. (2e)]. For x > 0.1 km, the pollutant near the ground becomes well-mixed, giving a uniform distribution with height. The vertical extent of this uniform concentration distribution increases with the downwind distance, while the magnitude of the concentration sharply decreases. The effect of the source height on the concentration profiles is negligible for x > 0.1 km.

Visibility is commonly defined as the greatest distance at which an observer can distinguish a contrast between an object and its background. Prevailing visibility (V_p) is the greatest visibility that is attained or

surpassed around at least half of the horizon, but not necessarily in continuous sectors. Degradation of visibility results from extraneous light which impinges on aerosols in the line of sight between target and observer, with subsequent scattering of a portion of this light toward the observer. The prevailing visibility in polluted air can be calculated as

$$V_p = \frac{K}{C} \tag{24a}$$

where V_p is the prevailing visibility (km), C is the mass concentration ($\mu g/m^3$) of particles in air, and K is a constant given as 1800 km-$\mu g/m^3$ (Williamson, 1973) based on data from various urban locations. The reduction in visibility, ΔV_p, due to an increase ΔC in the atmospheric concentration C of particles because of the fugitive dust emissions, can be derived from Eq. (24a) as

$$\Delta V_p = - \frac{K}{C^2} \cdot \Delta C \tag{24b}$$

Figure 5 also shows the visibilities calculated from Eq. (24) for Case I. In the near-field, the minimum visibility is under 100 m at elevations comparable to the source height. At ground level, the minimum visibility is of the order of 0.5 km. The visibility further decreases sharply with increasing relative humidities above 65%. Therefore, the fugitive coal dust emissions at Ravenswood Plant under conditions of high relative humidity might significantly reduce the prevailing visibilities in the vicinity of the plant, and impair navigation on the East River and transportation on nearby highways.

Figure 6 shows the vertical profiles of concentration and visibility for U = 4.5 m/s for Case II at five downwind locations. The results are similar to those shown for Case I, except that the concentrations are larger (and visibilities are smaller) due to the reduced turbulence levels and mixing depth for this case. The elevated peak concentration at x = 0.03 km is 3.4×10^{-2} g/m^3 and the corresponding visibility is about 50 m. At ground level, the minimum visibility is about 0.3 km.

7.3 Hourly Deposition Fluxes

The sector-average hourly deposition fluxes (kg/km^2/hr) at the surface for Case I are plotted in Fig. 7 as functions of the downwind distance and wind speed. Near the source, the deposition flux increases with distance from the source until it reaches a peak value, and then decreases following a single power law,

$$D_H(x) \propto x^{-n} \tag{25}$$

where $n \cong 2.2$ for all wind speeds. D_H depends on wind speed only in the near-field region, where the deposition flux increases as the wind speed decreases. The magnitude and location of the peak deposition flux vary as functions of the wind speed; for U = 1 m/s, a peak D_H of 5.6×10^5 kg/km^2/hr occurs at x = 30 m; for U = 14 m/s, the peak value is 3.5×10^3 kg/km^2/hr occurring at x = 70 m. For x > 2.1 km, the D_H values are less than 10 kg/km^2/hr. Thus the hourly surface deposition fluxes vary by several orders of magnitude over a downwind distance of 20 km from the source. It should be noted that D_H calculations are independent of the wind direction.

The sector-average hourly surface deposition fluxes for Cass II are shown in Fig. 8. The results are similar to those given for Case I, except that the peak D_H values are smaller at higher wind speeds, and occur at larger values of x in the near-field region. For x > 0.2 km, the D_H variation can be approximated by Eq. (25) with n $\cong$ 2.2 for all wind speeds.

7.4 Monthly Deposition Fluxes

The sector-average monthly surface-deposition fluxes (kg/km^2/month), D_M, are calculated from the hourly deposition fluxes by incorporating the climatological joint-frequency statistics of wind speed and direction at the site, and the pollutant loading factors, as described in Sect. 6.2. The monthly deposition fluxes are calculated over a distance of 0-20 km in each of the 16 wind direction sectors for each of the 12 months in a year, based on the site-meteorological data over five years (1974-1978).

Since the monthly deposition flux varies by several orders of magnitude over the downwind distance considered, the calculated results are presented as follows:

a) Near-Field Region: consists of the region x = 0 to 1 km. In this region, the isopleths of D_M = 5×10^5, 10^5, 5×10^4, 10^4, 5×10^3, and 10^3 kg/km^2/month are shown.

b) Far-Field Region: consists of the region x = 1 to 10 km. In this region, the isopleths of D_M = 10^3, 5×10^2, 10^2, 50, 10, and 5 kg/km^2/month are shown.

Thus, the deposition flux results for each month consist of two plots, one for the near-field and the other for the far-field region. To study the seasonal variation of the monthly deposition fluxes, the months were stratified by season, based on the average monthly temperature, and a

representative month was selected for each season as shown in Table 9.

The near and far-field results of monthly deposition fluxes for each of the four seasonally representative months are shown in Figs. 9 to 16 for Case I. Figures 9 and 10, respectively, show the near and far-field deposition flux isopleths for the month of January, representing the winter season. The contours are strongly peaked in the east-southeasterly (ESE) direction underlining the dominance of west-northwesterly winds prevailing at the site (see Table 4). Secondary peaks in D_M occur in the southwesterly and northerly directional sectors. The minimum deposition flux occurs in the northwesterly direction. The D_M values are less than 10^4 kg/km^2/month beyond 0.6 km and 100 kg/km^2/month beyond 5 km distance from the source. Except in the ENE to SSE quadrant, D_M is less than 5 kg/km^2/month beyond 10 km distance from the source.

The deposition flux isopleths for April (see Figs. 11 and 12), representing the spring season, are similar to January, except that the contours are more strongly peaked in the southeasterly direction and the secondary peaks are somewhat larger. The D_M values vary as indicated above for January. Except in the southeasterly direction, D_M is less than 10 kg/km^2/month beyond 10 km distance from the source.

The deposition flux isopleths for July (Figs. 13 and 14) are more evenly distributed around the source, except in the westerly direction. In addition to the prevailing westerly winds at the site, strong southerly and northeasterly winds are also frequent in summer, resulting in the marked peaks of D_M in the northerly and southwesterly directions. Except in the northerly direction, D_M is less than 5 kg/km^2/month beyond 10 km distance from the source.

The deposition flux isopleths for October (Figs. 15 and 16), representing the fall season, show the most evenly distributed contours in all directions except the NW quadrant. The D_M values are less than 10 kg/km^2/month at 10 km distance from the source in all directions.

The near and far-field results of monthly deposition fluxes for each of the four seasonally representative months are shown in Figs. 17 to 24 for Case II. For this case, the hourly meteorological data for all hours (both day and night) were included in the analyses. Based on a comparison of these deposition flux isopleths with the corresponding results for Case I, the following conclusions can be drawn:

a) The shape and orientation of the contours, resulting primarily from the wind directional bias, are similar for both cases. This implies that the strong daytime winds dominate the generally light nocturnal winds at the site, and the daytime wind direction and speed play a decisive role in determining the distribution of the surface deposition flux, on a monthly basis, around the source.

b) At any given surface location, the magnitudes of the deposition fluxes are larger for Case II than for Case I. The peak D_M values (in kg/km^2/month) for Case II are less than 5×10^4 beyond 0.5 km, 5×10^3 beyond 1.5 km, 5×10^2 beyond 3 km, and 50 beyond 7 km distance from the source. Except in a few directional sectors, D_M is well within 10 kg/km^2/month beyond 10 km.

c) Due to the dominance of prevailing winds at the site from the WSW-NNW quadrant, maximum deposition fluxes occur in the ENE-SSE quadrant. Secondary peaks are predicted in the northerly and

southwesterly sectors, especially in summer. The smallest deposition fluxes occur in the westerly and west-northwesterly sectors.

7.5 Yearly Deposition Fluxes

The sector-average yearly surface deposition fluxes ($kg/km^2/year$), D_y, are calculated from the hourly deposition fluxes by incorporating the yearly joint-frequency statistics of wind speed and direction at the site (see, Tables 5 and 7), and the pollutant loading factors, as described in Sect. 6.2. The yearly deposition fluxes are calculated over a distance of 0-20 km in each of the 16 wind direction sectors, based on the site-meteorological data over five years.

The near and far-field results of yearly deposition fluxes are shown Figs. 25 and 26, respectively, for Case I. The corresponding results for Case II are shown in Figs. 27 and 28. Based on a comparative study of the results, the following conclusions can be drawn:

a) The shape and orientation of the D_y contours are similar for both cases. This implies that the daytime wind frequency statistics play a dominant role in determining the distribution of the yearly deposition flux at the plant site.

b) For Case I, the D_y values (in $kg/km^2/year$) are less than 10^6 beyond 0.2 km, 10^5 beyond 0.6 km, 5×10^4 beyond 0.8 km, 10^4 beyond 1.7 km, 5×10^3 beyond 2.5 km, 10^3 beyond 5 km, 5×10^2 beyond 6 km, and 10^2 beyond 10 km distance from the source. For case II, the D_y values (in $kg/km^2/year$) are less then 10^6 beyond 0.3 km, 10^5 beyond 0.8 km, 5×10^4 beyond 1.1 km, 10^4 beyond 2.2 km, 5×10^3 beyond

3 km, 10^3 beyond 5 km, and 5×10^2 beyond 6 km, and 10^2 beyond 10 km distance from the source. Thus, at any given distance within 5 km, the magnitudes of the deposition fluxes are larger for Case II than for Case I.

c) Maximum yearly deposition fluxes occur in the ENE-SSE quadrant. Other peaks are predicted in the northerly and southwesterly sectors. The smallest deposition fluxes occur in the WSW-NNW quadrant.

The above results, except for the magnitudes, are similar to the conclusions drawn from the monthly deposition flux distributions. Thus one may conclude that the seasonal variations of meteorology do not significantly alter the predicted patterns of the pollutant particle — deposition flux in the vicinity of the Ravenswood plant.

7.6 Net Deposition Rates

The sector-average monthly net deposition rates (kg/month), N_M, between successive x locations in each wind direction sector for each month, are calculated from the monthly surface deposition flux array, D_M, as outlined in Sect. 6.2. As examples, the net deposition rates calculated for the month of January are shown in Tables 10 and 11 for Cases I and II, respectively. The value of N_M shown at each x_i in each sector is the amount of pollutant deposited during the month of January over the sector segment between x_i and x_{i-1}. The $N_M(x)$ variations shown in the Tables appear nonuniform since the distance increments between successive x locations were not uniform in this study.

The following conclusions can be drawn from the results. The largest values of N_M occur in the E, ESE, and SE sectors, and the smallest in the WNW, NW, and NNW sectors. These results are consistent with the D_M distributions discussed earlier. The N_M values for Case II are generally a factor of two larger than the corresponding Case I values. The largest net deposition rates occur in the near field due to the deposition of the large particles in the vicinity of the source. The peak values of N_M are 183 kg/month at x = 80 m for Case I and 405 kg/month at x = 100 m for Case II, both peaks occuring over a 22.5° sector segment of 10 m width in the easterly direction.

The total amount of the pollutant deposited per month within a distance of 20 km from the source can be obtained by summing up the N_M values at all x_i in all 16 sectors. This amount can be expressed as a percentage (P_m) of the total emission rate [see Eq. (21)]. The monthly P_m values range from 91 to 99 percent for Case I, and nearly 100 percent for Case II. Most of the deposition occurs within 10 km from the source.

The sector-average yearly net deposition rates (kg/year), N_y, between successive x locations in each wind direction sector are calculated from the yearly surface deposition flux array, D_y, as outlined in Sect. 6.2. The calculated N_y (x_i) for Cases I and II are shown in Tables 12 and 13, respectively. On an yearly basis, the maximum value of N_y is 1759 kg/year at x = 70 m for Case I, and 4171 kg/year at x = 80 m for Case II, both values calculated over a 22.5° sector segment of 10 m width in the northerly direction. The nearfield values of N_y in the N, E, ESE, SE and SW sectors are generally very large. The smallest values occur

in the WNW sector. The N_y values for Case II are about a factor of the two larger than the corresponding values for Case I.

The total amount of pollutant deposited per year within a distance of 20 km from the source can be obtained by summing up the N_y values at all x_i in all 16 sectors. This amount can be expressed as a percentage (P_y) of the total emission rate [see Eq. (22)]. The calculated P_y values are 98 percent for Case I and nearly 100 percent for Case II.

8. CONCLUSIONS AND RECOMMENDATIONS

The Ravenswood Power Plant of the Consolidated Edison Company of New York is being converted to use coal as the primary fuel. This study addressed the probable short and long-term air pollution impacts of the fugitive coal dust emissions from the facility. The major components and key assumptions of the study are as follows:

1. The coal is unloaded from the barges at a rate of 1255 tons/hr of which 0.01% was assumed to become airborne drift, giving a fugitive emission source strength (Q) of 31.6 g/s. This source, at a height h = 25 m, was assumed to be continuous, operating over the 13 daytime hours only (0700-1900 hrs) in Case I, and around the clock (both day and night) in Case II. Both cases were considered separately in this study.
2. The drift consists of particle sizes ranging from 0.1 to 200 μm. The drift particle size distributions by number or weight were assumed to be lognormal. Six ranges of particle sizes were considered, and each range was assigned a representative diameter, drift mass fraction, gravitational settling velocity, and depositon velocity.
3. Meteorological data used in this study consist of the five year (1974-78) record of hourly surface wind observations at the LaGuardia Airport NWS Station. Six wind speed classes and sixteen wind direction classes were considered. The meteorological data were analyzed for Cases I and II separately. Twelve monthly and one yearly arrays of joint-frequencies of wind speed and direction were generated for each case.

4. An atmospheric transport and diffusion model, consistent with the Gaussian plume assumptions, was formulated and applied to the present study. The calculated results of ground-level concentrations, atmospheric concentrations and visibilities, hourly surface deposition fluxes, and deposition flux and net deposition rates on monthly and yearly basis, were presented for Cases I and II separately.

The important results and conclusions of this study are the following:

1. The ground-level concentration (GLC) of the pollutant varies as a function of the downwind distance from the source (x) and the wind speed (U). The GLC increases as the wind speed decreases. Under very light wind conditions (U = 1 m/s), a maximum GLC of 0.1 g/m^3 occurs at x = 30 m for Case I, and 0.33 g/m^3 at x = 32 m for Case II. Under very gusty winds (U = 14 m/s), a maximum GLC of 7.7×10^{-4} g/m^3 occurs at x = 70 m for Case I, and 9.5×10^{-4} g/m^3 at x = 100 m for Case II. After the maximum is attained, the GLC decreases sharply as the distance increases. Thus, the maximum ground level concentrations in all cases occur in the vicinity of the plant.
2. The atmospheric concentration of the pollutant varies as a function of x, U, and the height (z) above the ground. For downwind distance of the order of a few tens of meters, the concentration profiles show the elevated peaks characteristic of the near-field diffusion from an elevated source. For x > 100 m, the pollutant near the ground becomes well-mixed, giving a uniform distribution with height. The

minimum prevailing visibility (V_p), which is inversely proportional to the maximum concentration, is of the order of 0.5 km for Case I and 0.3 km for Case II at the ground level. At elevations comparable to the source height, the minimum visibility in the near-field is under 100 m for Case I and 50 m for Case II. These values are further expected to decrease sharply with increasing relative humidities above 65%.

3. The sector-average hourly surface deposition flux, D_H, increases with x until it reaches a maximum value, and then decreases following a single power law, $D_H(x) \propto x^{-n}$, for all wind speeds. D_H depends on wind speed only in the vicinity of the source where D_H increases as wind speed decreases. In Case I, for U = 1 m/s, a maximum D_H of 5.6×10^5 kg/km^2/hr occurs at x = 30 m; for U = 14 m/s, the maximum is 3.5×10^3 kg/km^2/hr at x = 70 m. For x > 2.1 km, the D_H values are less than 10 kg/km^2/hr. The results for Case II also are similar except that the peak D_H values are smaller at higher wind speeds and occur at larger values of x in the vicinity of the source.

4. The sector-average monthly surface deposition flux, D_M, varies by several orders of magnitude over a distance of 20 km from the source. Due to the dominance of prevailing winds from the WSW-NNW quadrant at the site, maximum monthly deposition fluxes occur in the ENE-SSE quadrant. Secondary peaks are predicted in the northerly and southwesterly sectors, especially in summer. The smallest deposition fluxes occur in the westerly and west-northwesterly sectors. At any given x, the magnitudes of deposition fluxes are larger for Case II than for Case I. However, the shape and

orientation of the D_M contours, resulting from the wind directional bias, are similar for both cases. The deposition flux is less than 500 kg/km^2/month beyond 3 km, and 50 kg/km^2/month beyond 7 km distance from the source.

5. The results of the yearly deposition fluxes (D_y), except for their magnitudes, are similar to the D_M results. This suggests that the seasonal variations of meteorology do not significantly alter the predicted patterns of the pollutant deposition flux around the Ravenswood plant. For both cases, the predicted D_y values are less than 10^3 kg/km^2/year beyond 5 km, 500 kg/km^2/year beyond 6 km, and 100 kg/km^2/year beyond 10 km distance from the source.

6. The largest monthly net deposition rates (N_M) occur in the E, ESE, and SE sectors, and the smallest in the WNW, NW, and NNW sectors. The N_M values for Case II are generally a factor of two or more larger than the corresponding values for Case I. Similar results were also obtained for the yearly net deposition rates (N_y). On an yearly basis, the maximum value of N_y is 1759 kg/year at x = 70 m for Case I, and 4171 kg/year at x = 80 m for Case II, both values calculated over a 22.5° sector segment of 10 m width in the northerly direction. The total amount of the pollutant deposited per month within a distance of 20 km from the source ranges from 91 to 99 percent of pollutant emission rate for Case I, and nearly 100 percent for Case II. The corresponding yearly percentages are 98 and 100, respectively.

Some observations and recommendations based on the above results are given below.

1. For values of the fugitive emission source strength (Q) significantly different from the one used in this study, the concentrations and deposition fluxes can be obtained by simple multiplication of the present results by the appropriate source-scaling factor. Similarly, varying the time schedules for coal unloading, which might require significantly different values for the pollutant loading factors (P) from those used in this study, can be taken into account by appropriate scaling of the present results.
2. Since the source was assumed to be continuous, the results of this study are likely to provide a conservative worst-case estimate of the pollutant concentrations and deposition fluxes.
3. The fugitive coal dust emissions at Ravenswood plant under conditions of high relative humidity might seriously reduce the prevailing visibilities in the vicinity of the plant, and impair navigation on the East River and transportation on nearby highways. The predicted monthly deposition fluxes within 1 km of the source are large enough to require periodic dredging of the East River around the coal unloading tower.
4. The pollutant concentrations and deposition fluxes can be substantially reduced by using spill plates, screens, and other devices as drift eliminators, thereby reducing the drift emission rate. Pre-washing or spraying of the coal may reduce the coal fines that are more likely to become drift.

5. It is likely that some large particles with d > 200 μm, not included in the drift dispersion and deposition analyses, may also fall out during coal unloading. The deposition of these large particles, however, is nearly independent of the meteorological factors and occurs evenly around the source within a distance of 0.1 km. The total deposition flux in the immediate vicinity of the source, therefore, may be larger than calculated in this study.

REFERENCES

Briggs, G. A., 1973: Diffusion estimation for small emissions. *ATDL Contribution File No-79* (Draft), NOAA, Oak Ridge, TN, 59 pp.

Cadle, R. D., 1975: The measurement of airborne particles. John Wiley and Sons, New York, 342 pp.

Calder, K. L., 1961: Atmospheric diffusion of particulate material considered as a boundary value problem. *J. Meteorol.* 18, 413-416.

Carey, J. P., R. G. Ramsdell, C. F. Soutar and W. B. White, 1967: Ravenswood conversion to coal. Presented at American Power Conference, April 25-27, Chicago, 14 pp.

Chamberlain, A. C., 1953: Aspects of travel and deposition of aerosol and vapor clouds. *British Report AERE-HP/R-1261*, Harwell, U. K., 32 pp.

Ermak, D. L., 1977: An analytical model for pollutant transport and deposition from a point source. *Atmos. Environ.* 11, 231-237.

Fuchs, N. A., 1964: *The Mechanics of Aerosols*. The Macmillan Co., New York, 408 pp.

Gifford, F. A., 1976: Turbulent diffusion — typing schemes: A review. *Nuclear Safety* 17, 68-86.

Hatch, T., 1933: *J. Franklin Inst.* 215, p. 27.

Herdan, G., 1960: *Small Particle Statistics*. Academic Press, New York, 418 pp.

Holzworth, G. C., 1972: Mixing heights, wind speeds, and potential for urban air pollution throughout the contiguous United States. *Report AP-101*, Environmental Protection Agency, 118 pp.

Islitzer, N. F., and D. H. Slade, 1968: Diffusion and transport experiments. *Meteorology and Atomic Energy*, U.S. AEC, 117-188.

Lapple, C. E., 1961: *J. Stanford Res. Inst.* 5, p. 95.

McMahon, T. A., and P. J. Denison, 1979: Empirical atmospheric deposition parameters — A survey. *Atmos. Environ.* 13, 571-585.

Monin, A. S., 1959: On the boundary condition on the earth surface for diffusing pollution. *Adv. Geophys.* 6, 435-436.

Rao, K. S., 1975: Models for sulfur oxide dispersion from the Northport power station. The LILCO/Town of Huntington Sulfates Program. *Project Report P-1336*, Environmental Research & Technology, Inc., Concord, Mass.

Scriven, R. A., and B. E. A. Fisher, 1975: The long range transport of airborne material and its removal by deposition and washout. I & II. *Atmos. Environ.* 9, 49-68.

Sehmel, G. A., and W. H. Hodgson, 1974: Predicted dry deposition velocities. *Atmosphere — Surface Exchange of Particulate and Gaseous Pollutants*. R. J. Engelmann and G. A. Sehmel, Symposium Coordinators, Richland, WA; available as *Conf-740921* from NTIS, Springfield, VA, 399-423.

Sehmel, G. A., 1980: Particle and gas dry deposition: A review. Atmos. Environ. 14, 983-1011.

Smith, F. B., 1962: The problem of deposition in atmospheric diffusion of particulate matter. *J. Atmos. Sci.* 19, 429-434.

Smith, M. E., 1968: *Recommended Guide for the Prediction of the Dispersion of Airborne Effluents*. Amer. Soc. of Mech. Engrs., New York.

Turner, D. B., 1970: *Workbook of Atmospheric Dispersion Estimates*. Environmental Science Services Administration, U.S. Public Health Service, *Publication No. 999-AP-26*, 84 pp.

Williamson, S. J., 1973: *Fundamentals of Air Pollution*. Addison-Wesley Publishing Co., Reading, Mass., 472 pp.

Table 1. Coal drift mass distribution

i	Particle diameter range (microns)	Representative diameter d_i (microns)	Drift mass fraction f_i
1	< 5	3	.0006
2	5-10	8	.0020
3	10-30	20	.0263
4	30-60	45	.0974
5	60-100	80	.2026
6	100-200	150	.6711
Sum			1.0000

Table 2. Drift characteristics

i	Particle diameter d_i (microns)	Mass fraction f_i	Settling velocity W_i (cm/s)	Deposition velocity V_{di} (cm/s)
1	3	0.0006	0.07	0.80
2	8	0.0020	0.40	1.50
3	20	0.0263	2.70	2.70
4	45	0.0974	12.00	12.00
5	80	0.2026	32.00	32.00
6	150	0.6711	80.00	80.00

Table 3. Wind speed classification

Wind speed class	Wind speed range (mph)	Representative wind speed (m/s)
1	$0 \leq U \leq 3$	1
2	$3 < U \leq 7$	2.5
3	$7 < U \leq 12$	4.5
4	$12 < U \leq 18$	7
5	$18 < U \leq 24$	10
6	$24 < U$	14

TABLE 4. (CASE I) MONTHLY JOINT FREQUENCIES OF WIND SPEED AND WIND DIRECTION FOR THE MONTH OF JANUARY, 1974-78

WIND DIRECTION CLASS	WIND SPEED CLASS (MPH)					
	<=3	<=7	<=12	<=18	<=24	>24
N	0.0	0.0151	0.0238	0.0207	0.0032	0.0008
NNE	0.0	0.0103	0.0095	0.0079	0.0024	0.0008
NE	0.0	0.0183	0.0191	0.0207	0.0095	0.0032
ENE	0.0	0.0119	0.0231	0.0040	0.0008	0.0024
E	0.0	0.0024	0.0151	0.0008	0.0008	0.0
ESE	0.0	0.0024	0.0056	0.0016	0.0	0.0
SE	0.0	0.0024	0.0032	0.0016	0.0	0.0
SSE	0.0	0.0024	0.0056	0.0040	0.0	0.0
S	0.0	0.0056	0.0223	0.0191	0.0056	0.0008
SSW	0.0	0.0016	0.0135	0.0079	0.0032	0.0008
SW	0.0	0.0056	0.0318	0.0223	0.0056	0.0
WSW	0.0	0.0016	0.0159	0.0246	0.0159	0.0048
W	0.0	0.0111	0.0374	0.0962	0.0294	0.0032
WNW	0.0	0.0119	0.0477	0.0541	0.0374	0.0095
NW	0.0	0.0175	0.0397	0.0548	0.0223	0.0048
NNW	0.0	0.0103	0.0191	0.0231	0.0064	0.0008

TABLE 5. (CASE I) YEARLY JOINT FREQUENCIES OF WIND SPEED AND WIND DIRECTION FOR THE YEARS 1974-1978

WIND DIRECTION CLASS	WIND SPEED CLASS (MPH)					
	<=3	<=7	<=12	<=18	<=24	>24
N	0.0	0.0131	0.0221	0.0158	0.0026	0.0003
NNE	0.0001	0.0107	0.0151	0.0099	0.0015	0.0003
NE	0.0	0.0175	0.0360	0.0278	0.0099	0.0016
ENE	0.0	0.0139	0.0233	0.0140	0.0029	0.0006
E	0.0	0.0040	0.0093	0.0052	0.0008	0.0002
ESE	0.0	0.0031	0.0073	0.0020	0.0004	0.0001
SE	0.0	0.0040	0.0105	0.0051	0.0008	0.0001
SSE	0.0	0.0045	0.0154	0.0111	0.0013	0.0001
S	0.0	0.0083	0.0499	0.0523	0.0092	0.0013
SSW	0.0001	0.0063	0.0218	0.0146	0.0017	0.0001
SW	0.0	0.0063	0.0295	0.0264	0.0031	0.0
WSW	0.0	0.0068	0.0212	0.0231	0.0046	0.0005
W	0.0	0.0100	0.0355	0.0500	0.0165	0.0028
WNW	0.0	0.0118	0.0314	0.0417	0.0188	0.0039
NW	0.0	0.0145	0.0312	0.0448	0.0180	0.0033
NNW	0.0	0.0116	0.0184	0.0193	0.0051	0.0003

TABLE 6. (CASE II) MONTHLY JOINT FREQUENCIES OF WIND SPEED AND WIND DIRECTION FOR THE MONTH OF JANUARY, 1974-78

WIND DIRECTION CLASS	WIND SPEED CLASS (MPH)					
	<=3	<=7	<=12	<=18	<=24	>24
N	0.0	0.0208	0.0316	0.0199	0.0023	0.0005
NNE	0.0	0.0108	0.0122	0.0104	0.0014	0.0005
NE	0.0	0.0203	0.0176	0.0190	0.0086	0.0036
ENE	0.0005	0.0127	0.0194	0.0077	0.0014	0.0014
E	0.0	0.0063	0.0136	0.0018	0.0009	0.0
ESE	0.0	0.0041	0.0045	0.0018	0.0	0.0
SE	0.0	0.0045	0.0018	0.0014	0.0	0.0
SSE	0.0	0.0023	0.0036	0.0023	0.0	0.0005
S	0.0	0.0059	0.0167	0.0158	0.0045	0.0009
SSW	0.0	0.0050	0.0158	0.0081	0.0018	0.0014
SW	0.0	0.0059	0.0298	0.0199	0.0041	0.0009
WSW	0.0	0.0050	0.0145	0.0240	0.0145	0.0059
W	0.0	0.0131	0.0407	0.0967	0.0420	0.0059
WNW	0.0	0.0095	0.0420	0.0488	0.0330	0.0099
NW	0.0	0.0136	0.0366	0.0506	0.0199	0.0068
NNW	0.0	0.0081	0.0194	0.0212	0.0095	0.0005

TABLE 7. (CASE II) YEARLY JOINT FREQUENCIES OF WIND SPEED AND WIND DIRECTION FOR THE YEARS 1974-1978

WIND DIRECTION CLASS	WIND SPEED CLASS (MPH)					
	<=3	<=7	<=12	<=18	<=24	>24
N	0.0	0.0170	0.0251	0.0154	0.0021	0.0003
NNE	0.0	0.0125	0.0166	0.0103	0.0016	0.0002
NE	0.0	0.0183	0.0330	0.0246	0.0089	0.0017
ENE	0.0	0.0158	0.0199	0.0121	0.0030	0.0010
E	0.0	0.0063	0.0097	0.0044	0.0007	0.0001
ESE	0.0	0.0050	0.0062	0.0016	0.0003	0.0
SE	0.0	0.0063	0.0097	0.0033	0.0006	0.0001
SSE	0.0	0.0075	0.0132	0.0070	0.0008	0.0001
S	0.0	0.0167	0.0477	0.0364	0.0059	0.0009
SSW	0.0	0.0137	0.0282	0.0143	0.0014	0.0001
SW	0.0	0.0127	0.0356	0.0253	0.0027	0.0002
WSW	0.0	0.0106	0.0241	0.0204	0.0047	0.0008
W	0.0	0.0127	0.0381	0.0474	0.0154	0.0026
WNW	0.0	0.0127	0.0319	0.0388	0.0163	0.0035
NW	0.0	0.0123	0.0288	0.0389	0.0155	0.0031
NNW	0.0	0.0110	0.0202	0.0204	0.0053	0.0004

Table 8. Values of coefficients in Briggs' (1973) formulas for $\sigma_y(x)$ and $\sigma_z(x)$ in urban conditions

PG stability class	Description	a_y	a_z	b_z	c_z
A	Extremely unstable	.32	.24	.001	.001
B	Moderately unstable	.32	.24	.001	.001
C	Slightly unstable	.22	.20	0	0
D	Neutral	.16	.14	.0003	0
E	Slightly stable	.11	.08	.0015	0
F	Moderately stable	.11	.08	.0015	0

Table 9. Seasonal stratification of months

Season	Months	Average monthly temperature (°C)	Representative month
Winter	December	0.2	January
	January		
	February		
Spring	March	11.3	April
	April		
	May		
Summer	June	22.8	July
	July		
	August		
Fall	September	13.5	October
	October		
	November		

TABLE 10

(CASE I)

JANUARY

NET DEPOSITION RATE (KG/MONTH)

X(KM)	N	NNE	NE	ENE	E	ESE	SE	SSE
0.01	0	0	0	0	0	0	0	0
0.03	5	2	5	2	11	11	14	7
0.05	46	21	56	34	116	113	117	59
0.07	67	32	83	57	181	170	166	80
0.09	62	30	78	57	175	163	154	72
0.20	405	202	506	392	1183	1082	1001	460
0.40	131	66	163	137	405	365	327	146
0.60	74	37	93	79	232	208	186	83
0.80	51	26	64	54	160	143	128	57
1.00	39	19	48	41	120	108	97	43
1.20	31	15	38	32	96	86	77	34
1.40	26	13	33	27	81	73	66	29
1.60	24	12	30	25	75	68	60	26
1.80	22	11	27	24	70	62	55	24
2.00	20	10	25	22	65	58	50	22
3.00	71	36	87	85	243	214	183	77
4.00	46	23	56	60	169	148	124	50
6.00	48	24	57	69	187	166	135	53
8.00	25	13	29	39	100	93	73	28
10.00	15	8	17	24	60	57	44	17
12.00	10	5	11	15	39	37	29	11
14.00	7	3	8	11	28	26	21	8
16.00	5	2	6	8	21	19	15	6
18.00	4	2	4	6	16	15	12	4
20.00	3	1	3	5	13	12	9	3

TABLE 10

(CASE I)

JANUARY

NET DEPOSITION RATE (KG/MONTH)

X(KM)	S	SSW	SW	WSW	W	WNW	NW	NNW
0.01	0	0	0	0	0	0	0	0
0.03	10	6	12	8	2	1	1	1
0.05	75	42	82	57	21	12	10	13
0.07	97	51	104	72	30	16	12	18
0.09	85	44	90	62	27	14	11	16
0.20	529	265	560	378	169	87	66	101
0.40	161	78	171	111	52	25	19	31
0.60	91	44	97	62	29	14	10	17
0.80	63	30	67	43	20	10	7	12
1.00	48	23	51	33	15	7	5	9
1.20	38	18	41	26	12	6	4	7
1.40	32	15	34	22	10	5	3	6
1.60	29	14	31	19	9	4	3	5
1.80	26	12	28	17	8	4	3	5
2.00	23	11	25	15	7	3	2	4
3.00	79	36	87	50	24	11	8	15
4.00	50	23	57	30	14	7	5	9
6.00	51	23	61	29	13	6	4	9
8.00	26	12	33	15	6	3	2	4
10.00	16	7	20	9	4	2	1	2
12.00	10	5	13	6	2	1	1	1
14.00	7	3	9	4	1	0	0	1
16.00	5	2	7	3	1	0	0	1
18.00	4	2	5	2	1	0	0	0
20.00	3	1	4	2	0	0	0	0

TABLE 11

(CASE II)

JANUARY

NET DEPOSITION RATE (KG/MONTH)

X(KM)	N	NNE	NE	ENE	E	ESE	SE	SSE
0.01	0	0	0	0	0	0	0	0
0.03	0	0	0	0	0	0	0	0
0.05	40	34	46	35	97	74	94	54
0.07	120	101	151	114	327	251	286	158
0.09	121	99	168	130	396	301	304	157
0.20	861	674	1236	1038	3274	2417	2279	1117
0.40	272	197	387	388	1244	883	785	361
0.60	141	101	199	211	675	475	418	190
0.80	93	65	129	141	451	317	277	125
1.00	68	47	94	105	335	235	205	92
1.20	53	37	73	83	265	185	161	72
1.40	43	30	60	68	217	152	132	59
1.60	36	25	50	58	184	129	111	49
1.80	31	21	43	50	159	111	96	42
2.00	27	18	37	44	139	98	84	37
3.00	79	53	106	137	428	301	255	110
4.00	42	28	56	78	236	170	140	59
6.00	38	26	50	72	211	157	128	53
8.00	19	13	26	37	108	79	65	27
10.00	12	8	15	22	66	48	39	16
12.00	8	5	10	15	44	32	26	11
14.00	5	3	7	10	31	23	19	7
16.00	4	2	5	8	23	17	14	5
18.00	3	2	4	6	18	13	10	4
20.00	2	1	3	4	14	10	8	3

TABLE 11

(CASE II)

JANUARY

NET DEPOSITION RATE (KG/MONTH)

X(KM)	S	SSW	SW	WSW	W	WNW	NW	NNW
0.01	0	0	0	0	0	0	0	0
0.03	0	0	0	20	0	0	0	0
0.05	128	65	120	87	40	24	25	14
0.07	336	165	301	204	107	60	59	37
0.09	280	132	237	166	91	46	40	31
0.20	1682	776	1398	974	544	252	192	190
0.40	442	203	388	246	133	58	38	50
0.60	223	103	201	123	65	28	18	25
0.80	143	66	132	79	41	18	11	16
1.00	104	48	97	57	29	13	8	12
1.20	80	37	76	44	22	10	6	9
1.40	65	30	62	35	18	8	5	7
1.60	54	25	52	30	15	6	4	6
1.80	46	22	45	25	13	5	3	5
2.00	40	19	39	22	11	4	3	4
3.00	113	54	118	62	30	13	9	13
4.00	58	28	65	33	15	6	4	7
6.00	53	25	60	30	14	6	4	6
8.00	27	13	30	15	7	3	2	3
10.00	16	8	18	9	4	1	1	2
12.00	11	5	12	6	2	1	0	1
14.00	7	3	8	4	2	0	0	0
16.00	5	2	6	3	1	0	0	0
18.00	4	2	5	2	1	0	0	0
20.00	3	1	4	2	0	0	0	0

TABLE 12

(CASE I)

YEARLY NET DEPOSITION RATE

(KG / YEAR)

X(KM)	N	NNE	NE	ENE	E	ESE	SE	SSE
0.01	0	0	0	0	0	0	0	0
0.03	115	86	76	71	115	121	140	100
0.05	1163	557	703	614	1072	1053	1157	730
0.07	1759	766	1027	877	1595	1524	1640	964
0.09	1667	696	956	810	1507	1423	1516	855
0.20	10944	4417	6181	5218	9918	9286	9816	5342
0.40	3614	1390	1999	1685	3300	3063	3207	1658
0.60	2058	789	1136	958	1883	1747	1828	941
0.80	1419	544	784	661	1298	1205	1261	650
1.00	1073	413	593	501	982	912	955	493
1.20	857	331	474	400	784	729	763	396
1.40	727	280	402	339	665	618	648	335
1.60	668	253	367	310	612	567	592	302
1.80	612	229	335	282	563	521	543	273
2.00	562	208	305	258	518	478	497	246
3.00	2007	712	1071	910	1881	1734	1791	847
4.00	1322	449	691	596	1274	1179	1212	547
6.00	1369	445	697	619	1377	1294	1323	568
8.00	716	229	359	324	740	706	717	299
10.00	428	137	214	194	445	428	433	179
12.00	285	91	142	129	295	283	287	119
14.00	204	65	102	92	210	201	204	85
16.00	153	49	76	69	157	150	153	63
18.00	119	38	59	53	122	117	118	49
20.00	95	30	47	42	97	93	94	39

TABLE 12

(CASE I)

YEARLY NET DEPOSITION RATE

(KG / YEAR)

X(KM)	S	SSW	SW	WSW	W	WNW	NW	NNW
0.01	0	0	0	0	0	0	0	0
0.03	113	108	159	119	36	28	37	47
0.05	798	608	1197	831	275	202	287	394
0.07	1032	758	1605	1067	364	262	384	551
0.09	903	654	1435	929	322	228	341	502
0.20	5562	3978	9007	5699	2004	1399	2121	3188
0.40	1687	1185	2811	1717	613	418	650	1007
0.60	955	670	1595	972	347	236	368	571
0.80	660	463	1102	672	240	163	254	394
1.00	502	352	836	511	182	124	193	299
1.20	403	283	670	410	146	99	155	239
1.40	341	240	568	347	124	84	131	203
1.60	305	213	513	310	111	75	117	184
1.80	274	190	464	277	100	67	105	166
2.00	245	170	419	248	90	59	95	151
3.00	820	558	1443	825	301	194	318	519
4.00	513	345	931	513	187	116	196	329
6.00	513	343	967	512	185	111	192	328
8.00	266	177	514	267	96	57	99	169
10.00	160	107	311	161	58	34	59	101
12.00	106	71	207	108	38	23	40	67
14.00	76	51	147	77	27	16	28	48
16.00	57	38	110	57	20	12	21	36
18.00	44	29	85	44	16	9	16	28
20.00	35	23	68	35	12	7	13	22

TABLE 13

(CASE II)

YEARLY NET DEPOSITION RATE

(KG / YEAR)

X(KM)	N	NNE	NE	ENE	E	ESE	SE	SSE
0.01	0	0	0	0	0	0	0	0
0.03	3	3	2	2	2	2	2	2
0.05	1392	1070	1052	850	1091	1052	1009	857
0.07	4057	2898	3040	2395	3342	3113	2970	2353
0.09	3993	2549	2950	2260	3563	3189	3027	2150
0.20	27298	15845	19868	15143	26395	23168	22006	14172
0.40	8165	4238	5807	4525	8839	7728	7383	4239
0.60	4193	2129	2964	2335	4667	4093	3917	2195
0.80	2727	1369	1921	1523	3079	2706	2592	1435
1.00	1987	990	1396	1112	2267	1995	1912	1050
1.20	1547	766	1085	867	1778	1567	1503	820
1.40	1257	620	880	706	1454	1283	1231	668
1.60	1052	517	736	592	1225	1082	1038	561
1.80	901	441	629	507	1053	931	894	481
2.00	784	382	547	442	921	815	783	420
3.00	2231	1061	1539	1274	2730	2442	2347	1218
4.00	1163	543	793	673	1473	1337	1283	645
6.00	1044	490	710	605	1322	1209	1157	576
8.00	540	253	368	312	680	620	593	297
10.00	328	153	223	189	414	376	360	180
12.00	219	102	149	126	276	251	241	120
14.00	155	72	105	89	197	179	171	85
16.00	115	53	78	66	146	133	128	63
18.00	88	40	59	51	113	103	98	49
20.00	69	32	47	40	89	81	78	38

TABLE 13

(CASE II)

YEARLY NET DEPOSITION RATE

(KG / YEAR)

X(KM)	S	SSW	SW	WSW	W	WNW	NW	NNW
0.01	0	0	0	0	0	0	0	0
0.03	3	2	4	3	1	1	1	1
0.05	1275	927	1413	1166	473	366	472	573
0.07	3318	2383	3824	2981	1229	919	1219	1521
0.09	2747	1931	3397	2397	1010	708	989	1296
0.20	16374	11309	21776	13986	5934	3883	5720	7870
0.40	4279	2910	6295	3621	1505	892	1408	2070
0.60	2155	1464	3244	1830	752	437	698	1040
0.80	1388	943	2116	1183	482	277	446	669
1.00	1006	683	1546	859	348	199	321	484
1.20	780	530	1206	667	269	153	248	374
1.40	632	429	982	541	218	123	200	303
1.60	528	358	824	453	181	102	166	253
1.80	450	306	706	387	155	87	142	215
2.00	391	266	616	337	134	75	123	187
3.00	1099	749	1790	961	374	205	339	521
4.00	569	388	958	508	193	105	174	268
6.00	512	350	869	463	175	96	159	242
8.00	265	180	446	238	90	49	82	125
10.00	160	109	269	143	54	29	49	75
12.00	106	72	180	95	36	19	32	50
14.00	75	51	127	67	25	13	23	35
16.00	55	38	95	50	18	10	17	26
18.00	43	29	73	38	14	7	13	20
20.00	34	23	57	30	11	6	10	15

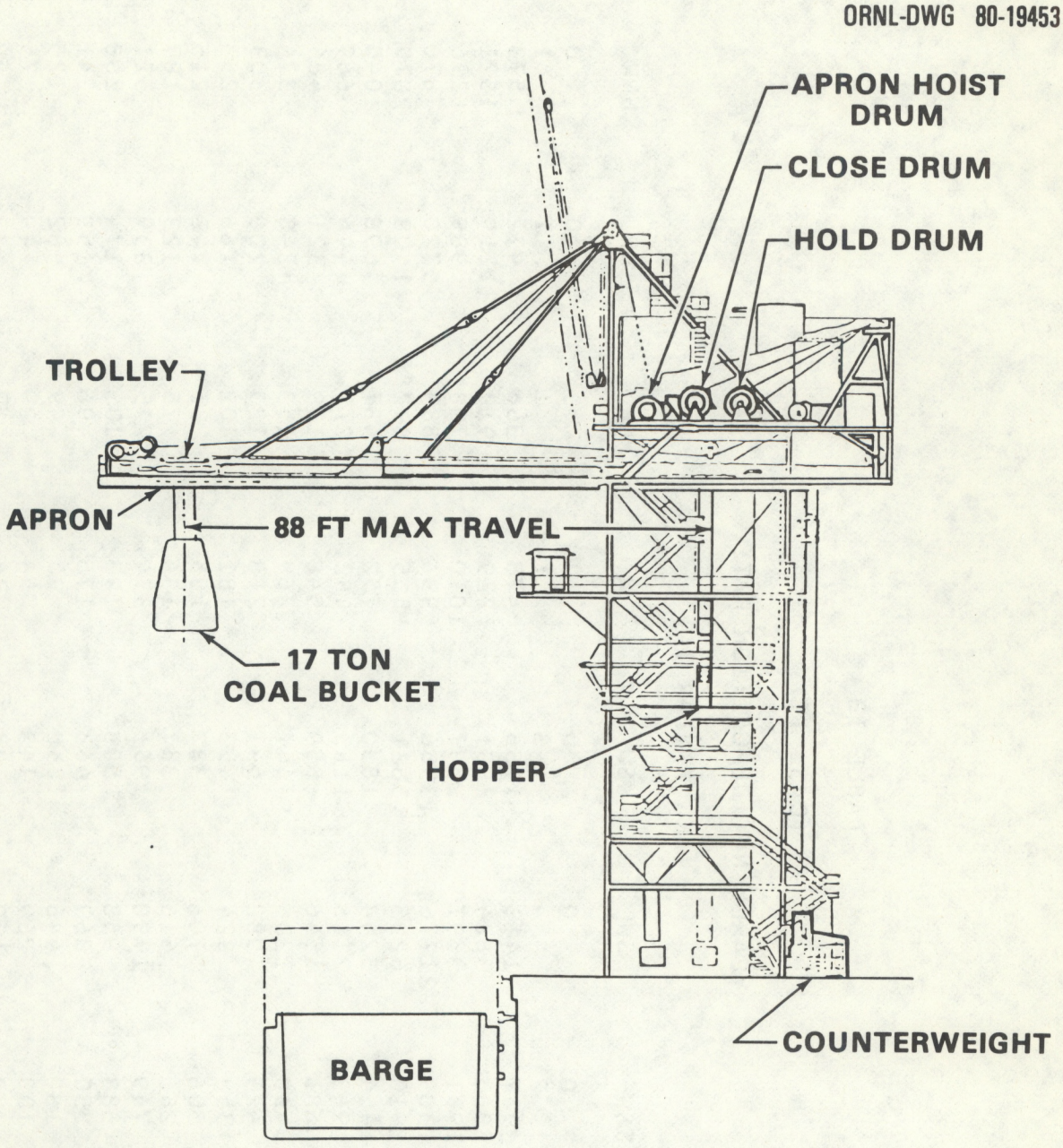

Figure 1. Stationary coal unloading tower.

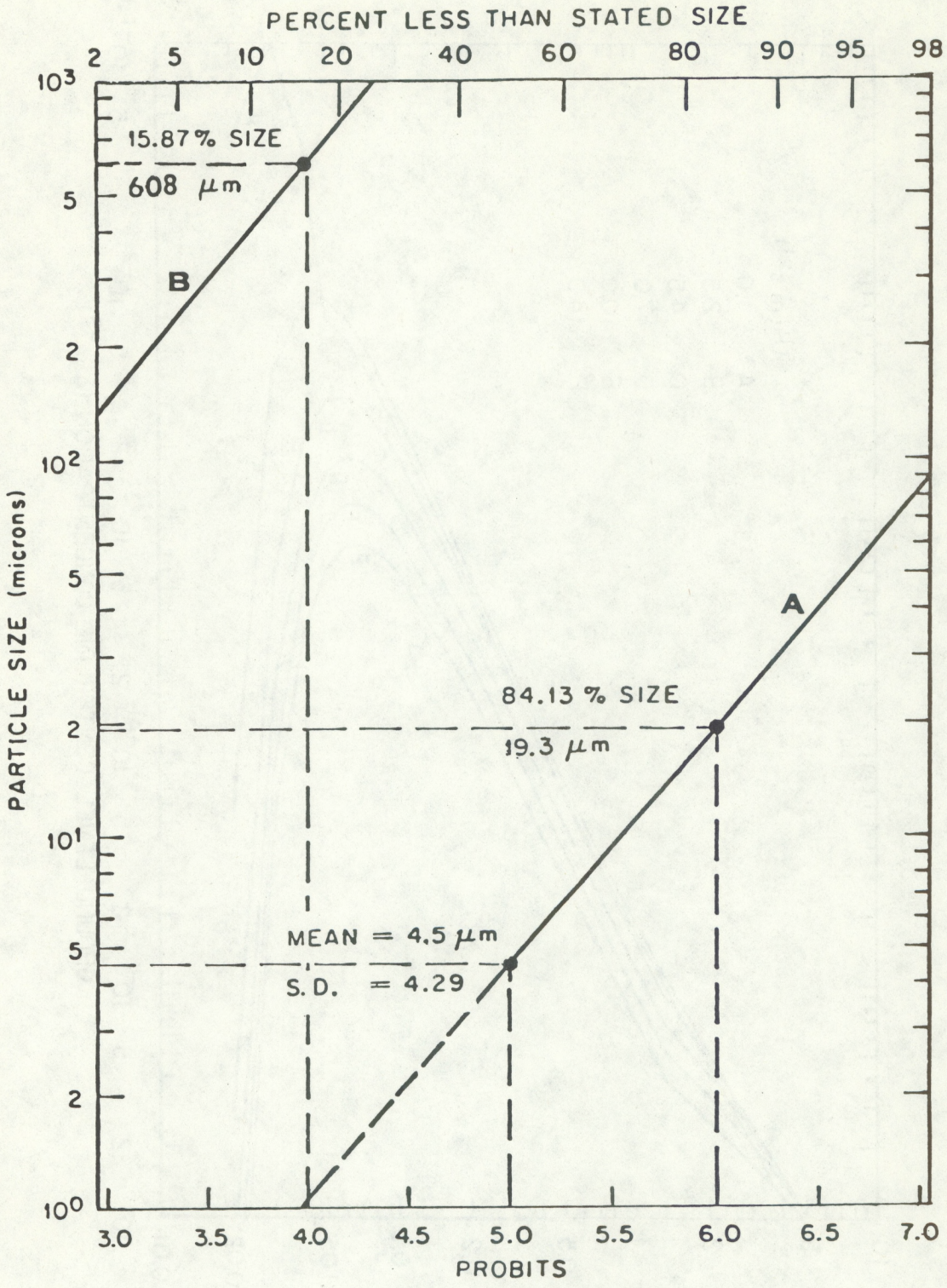

Figure 2. Lognormal probability plot of particle size distributions by number (line A) and by weight (Line B) for Wyoming coal.

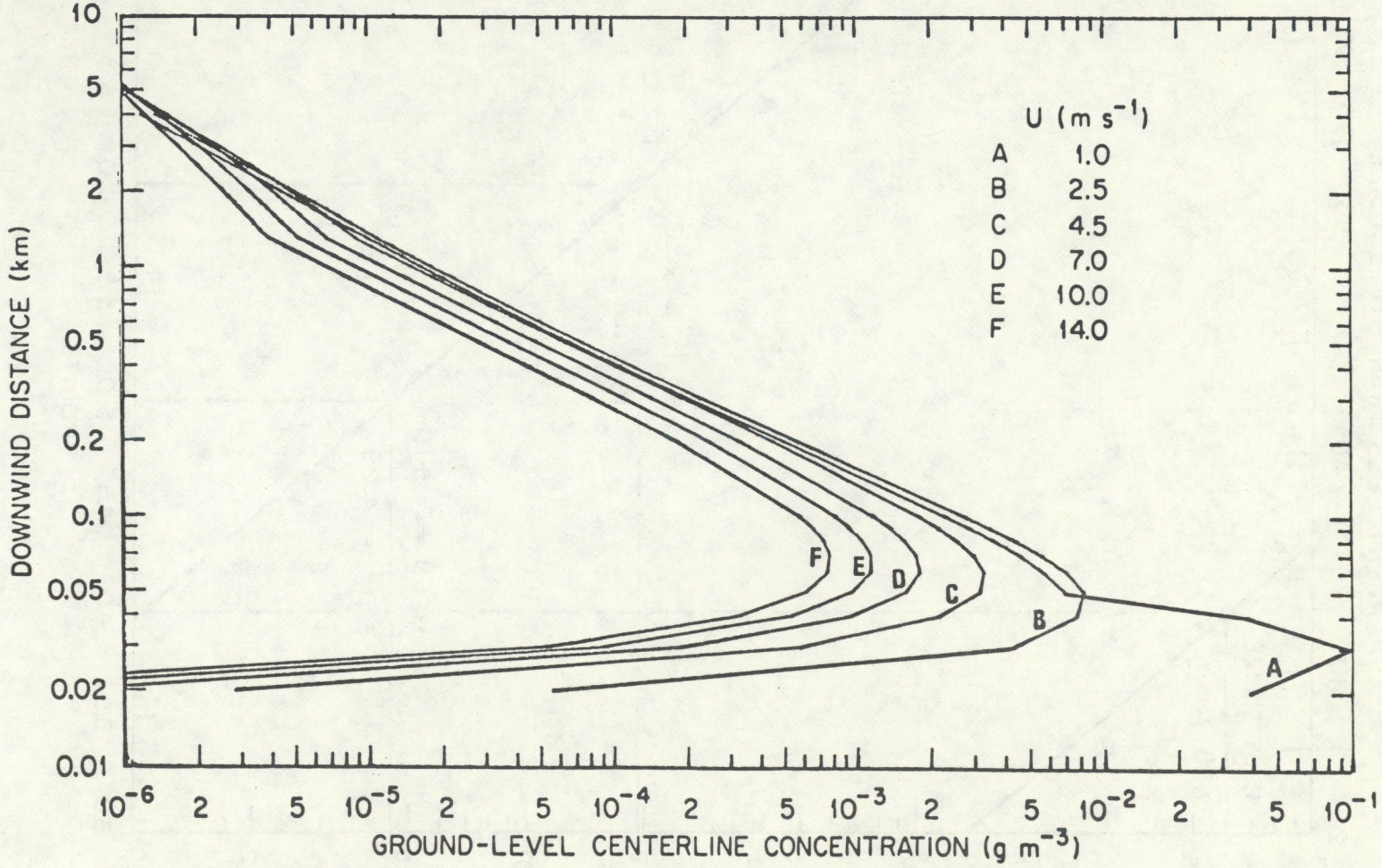

Figure 3. Variation of ground-level centerline concentration with downwind distance, shown as a function of wind speed, for Case I.

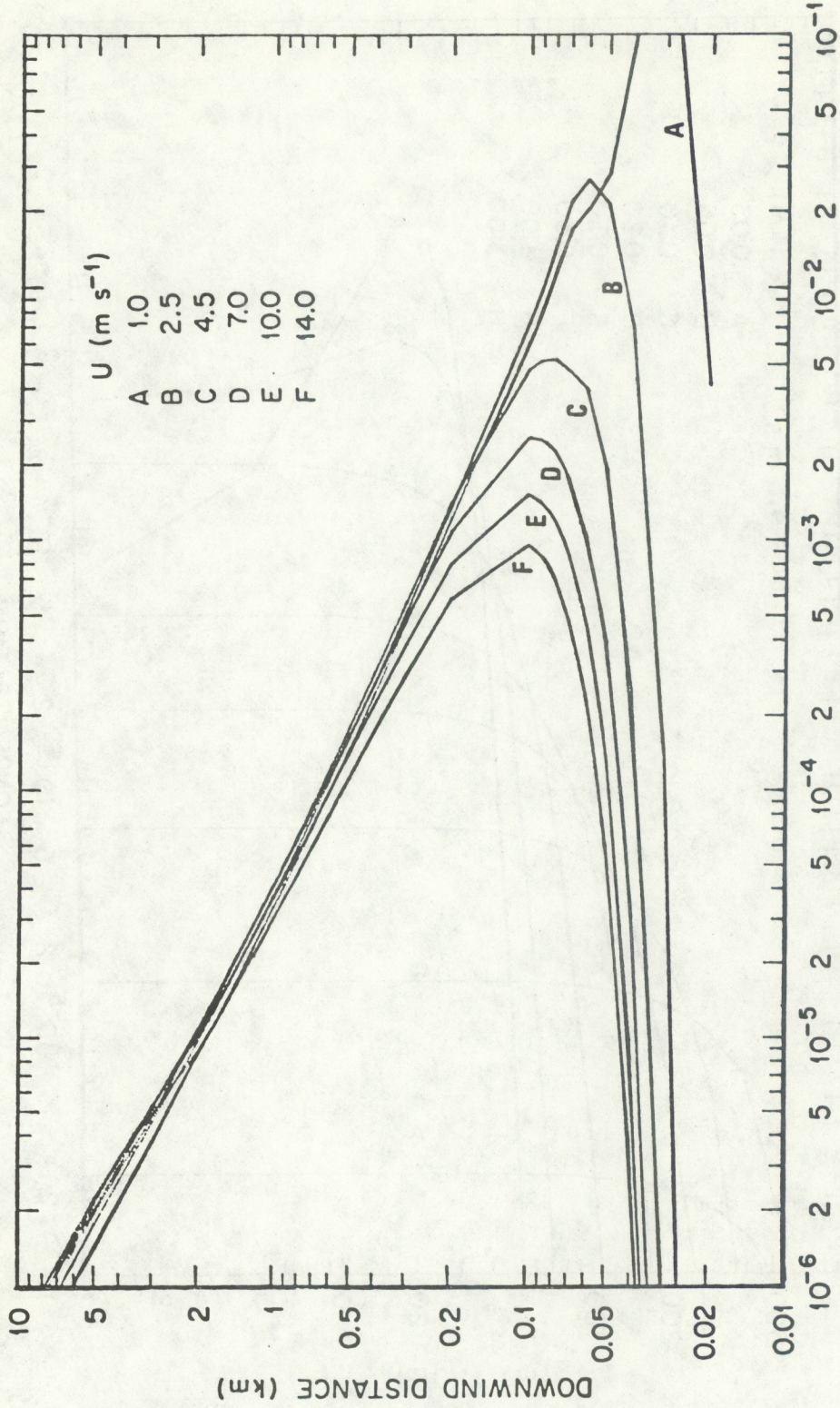

Figure 4. Variation of ground-level centerline concentration with downwind distance, shown as a function of wind speed, for Case II.

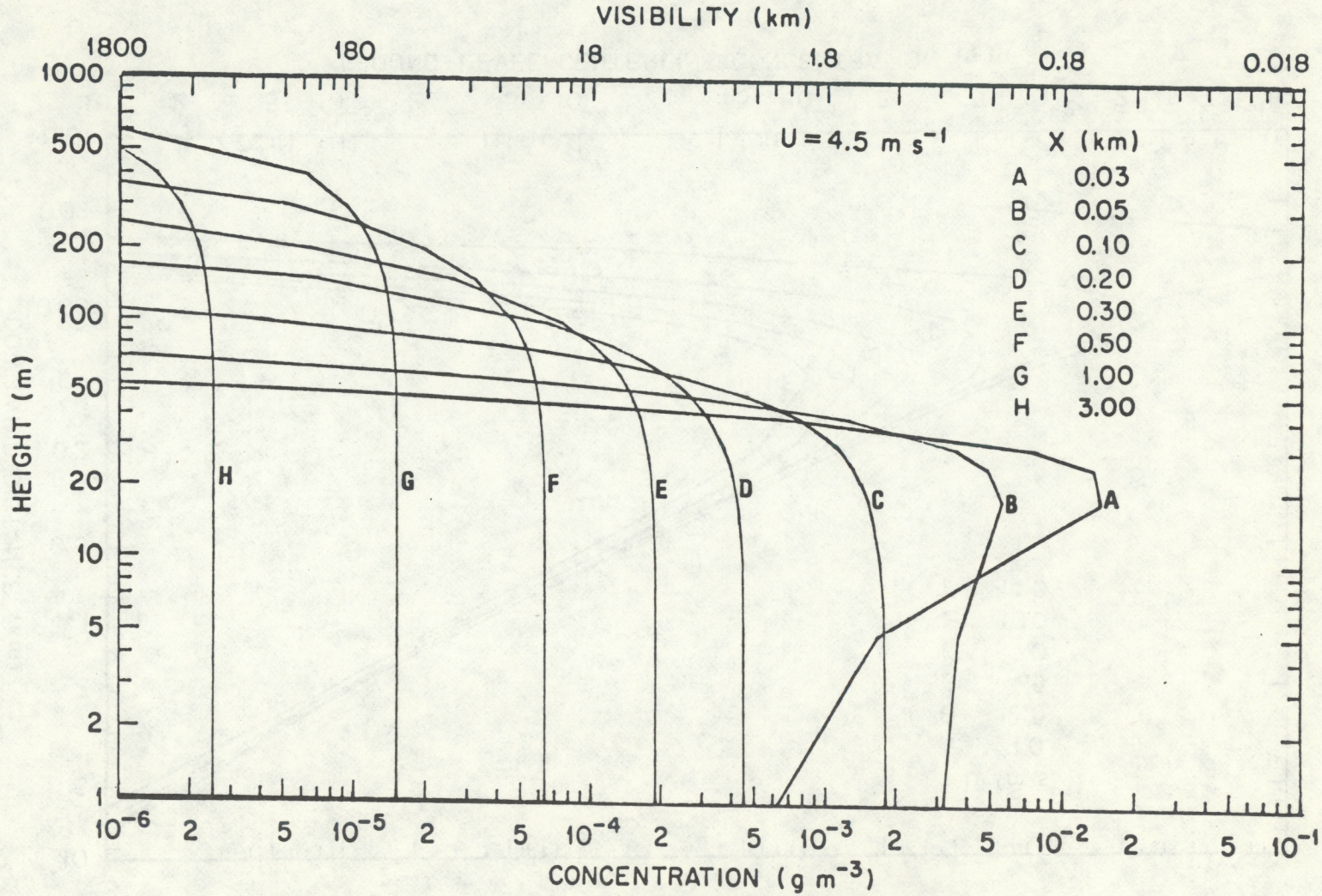

Figure 5. Vertical profiles of atmospheric concentration and visibility at several downwind distances (Case I).

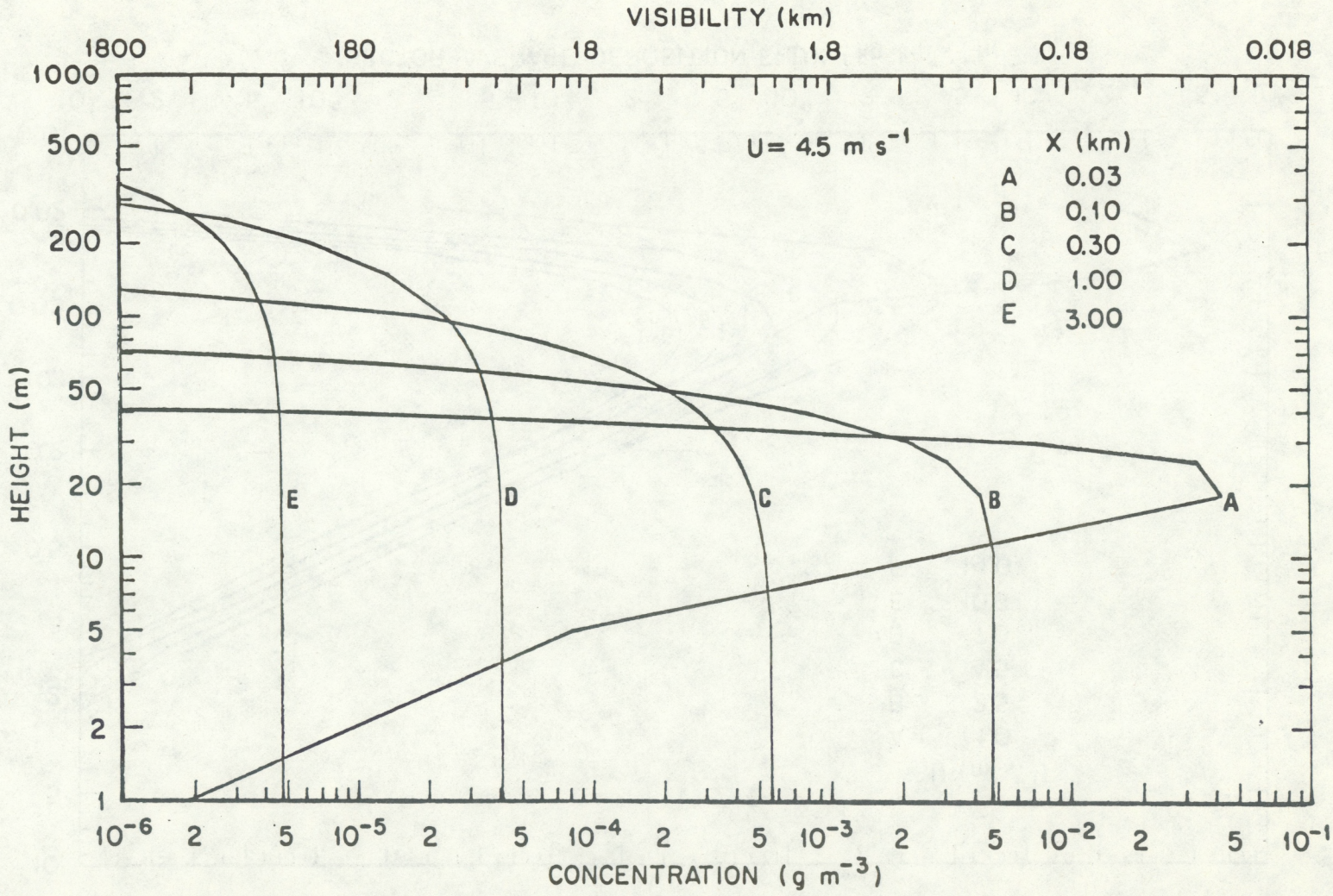

Figure 6. Vertical profiles of atmospheric concentration and visibility at several downwind distances (Case II).

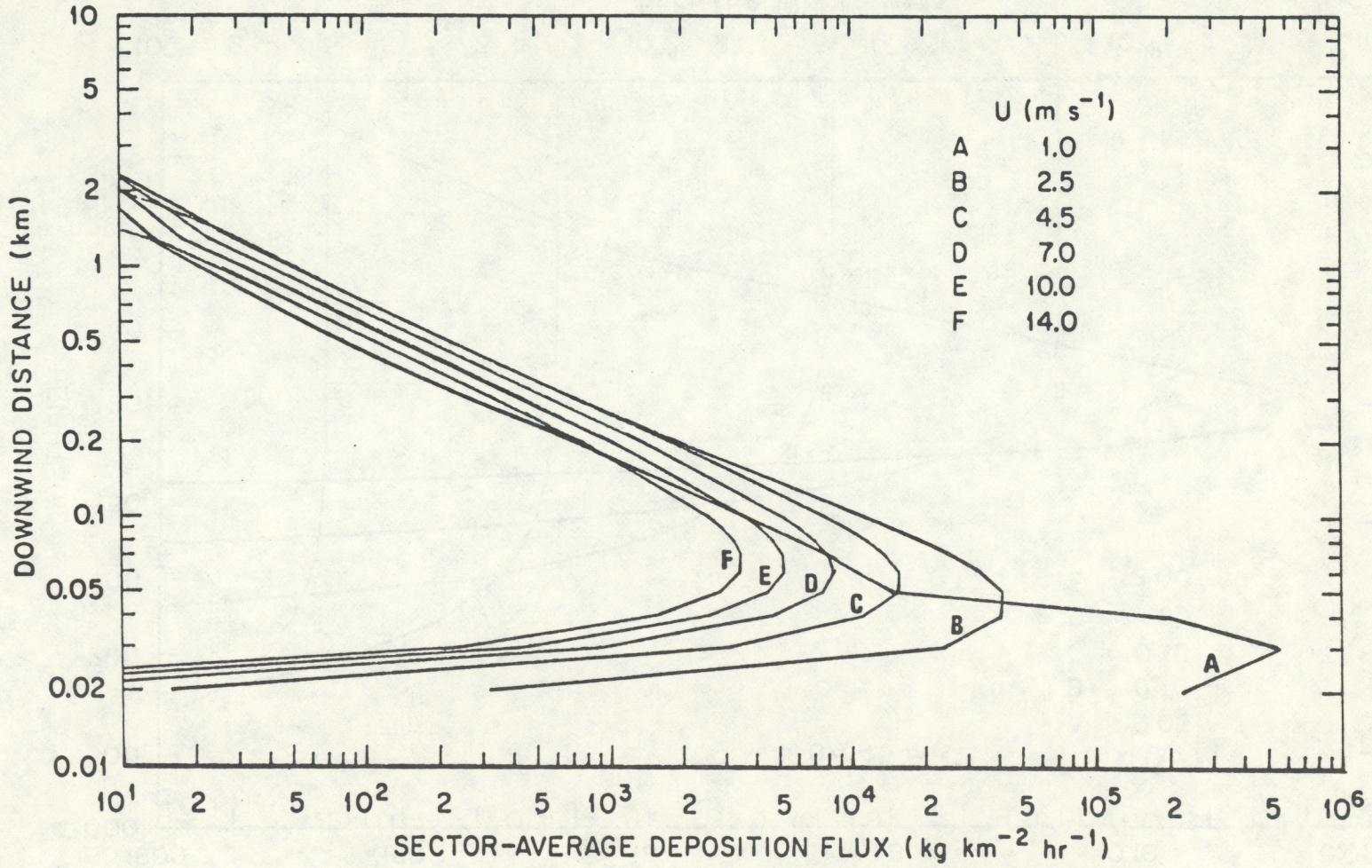

Figure 7. Variation of sector-average hourly surface deposition flux with downwind distance, shown as a function of wind speed, for Case I.

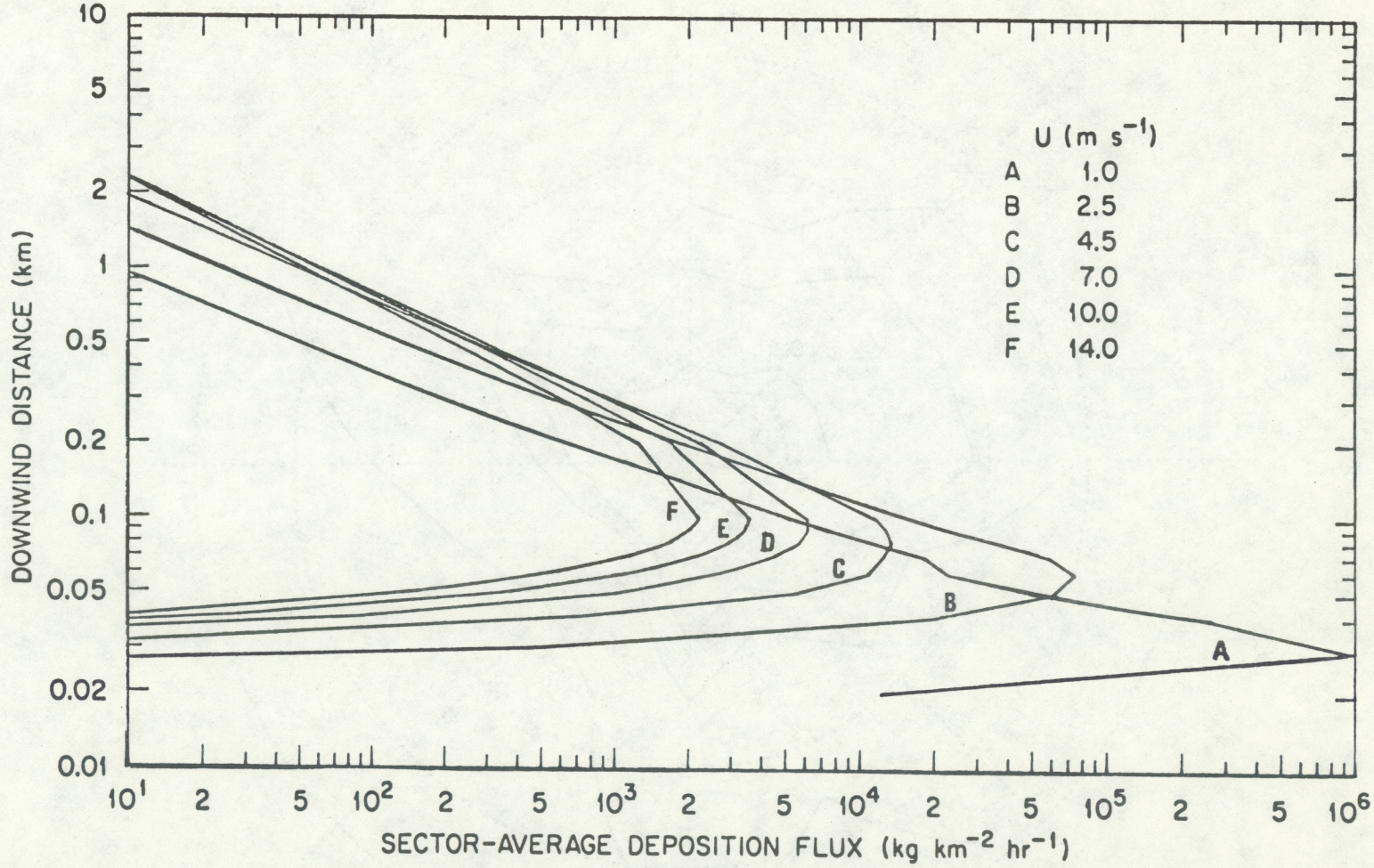

Figure 8. Variation of sector-average hourly surface deposition flux with downwind distance, shown as a function of wind speed, for Case II.

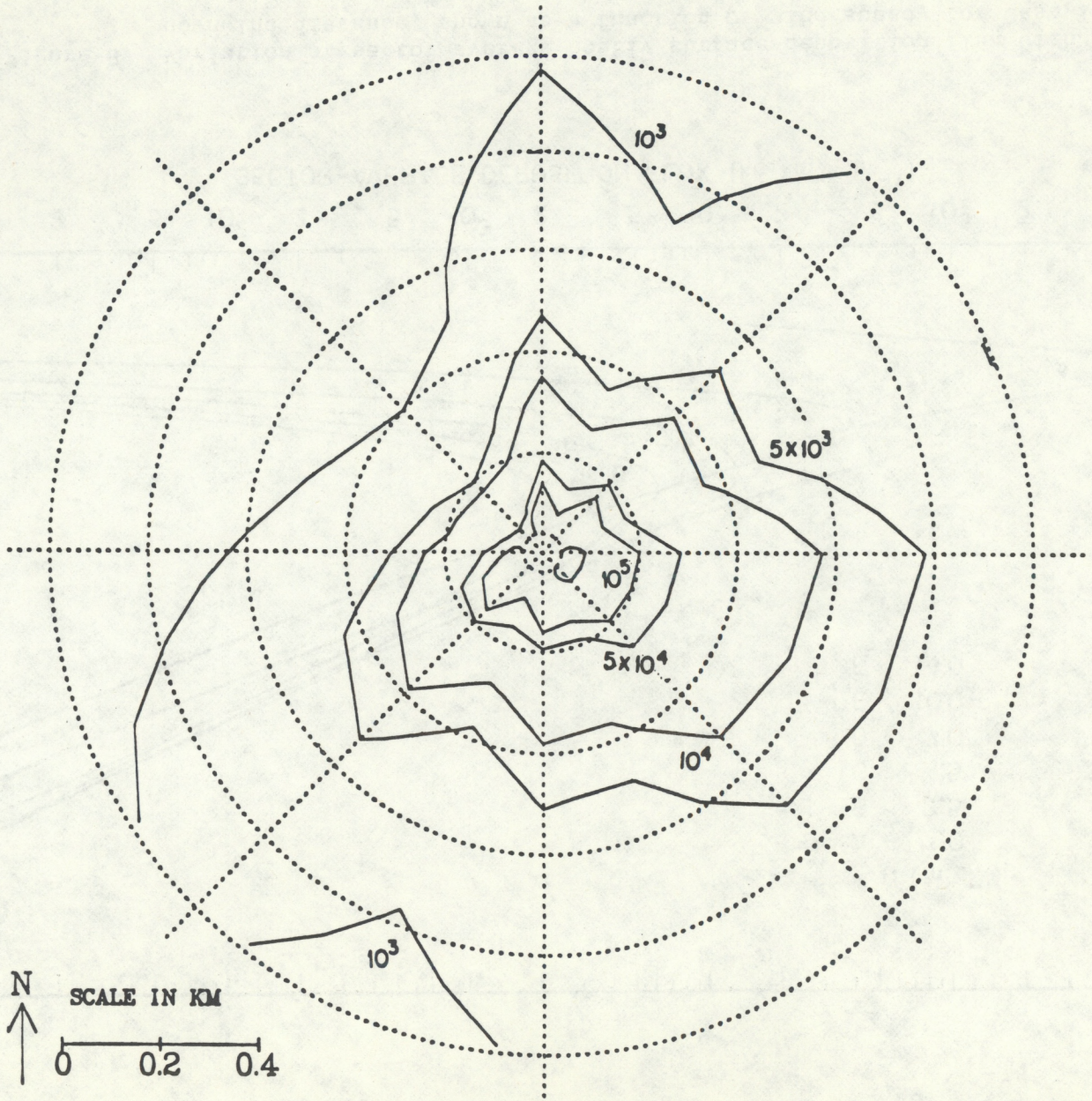

Figure 9. Isopleths of sector-average monthly surface deposition flux (kg/km^2/month) in the near-field region for the month of January (Case I).

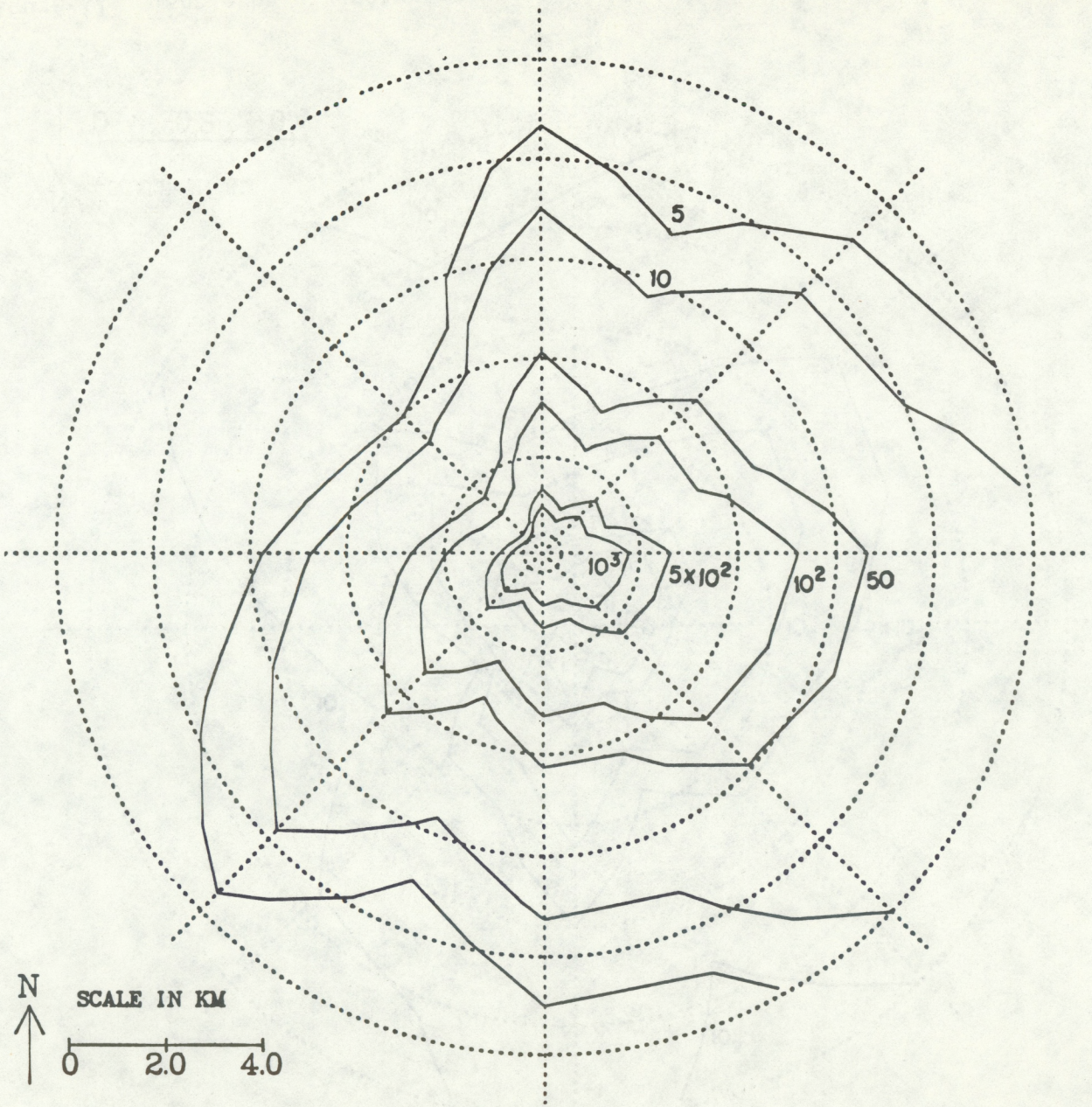

Figure 10. Isopleths of sector-average monthly surface deposition flux (kg/km^2/month) in the far-field region for the month of January (Case I).

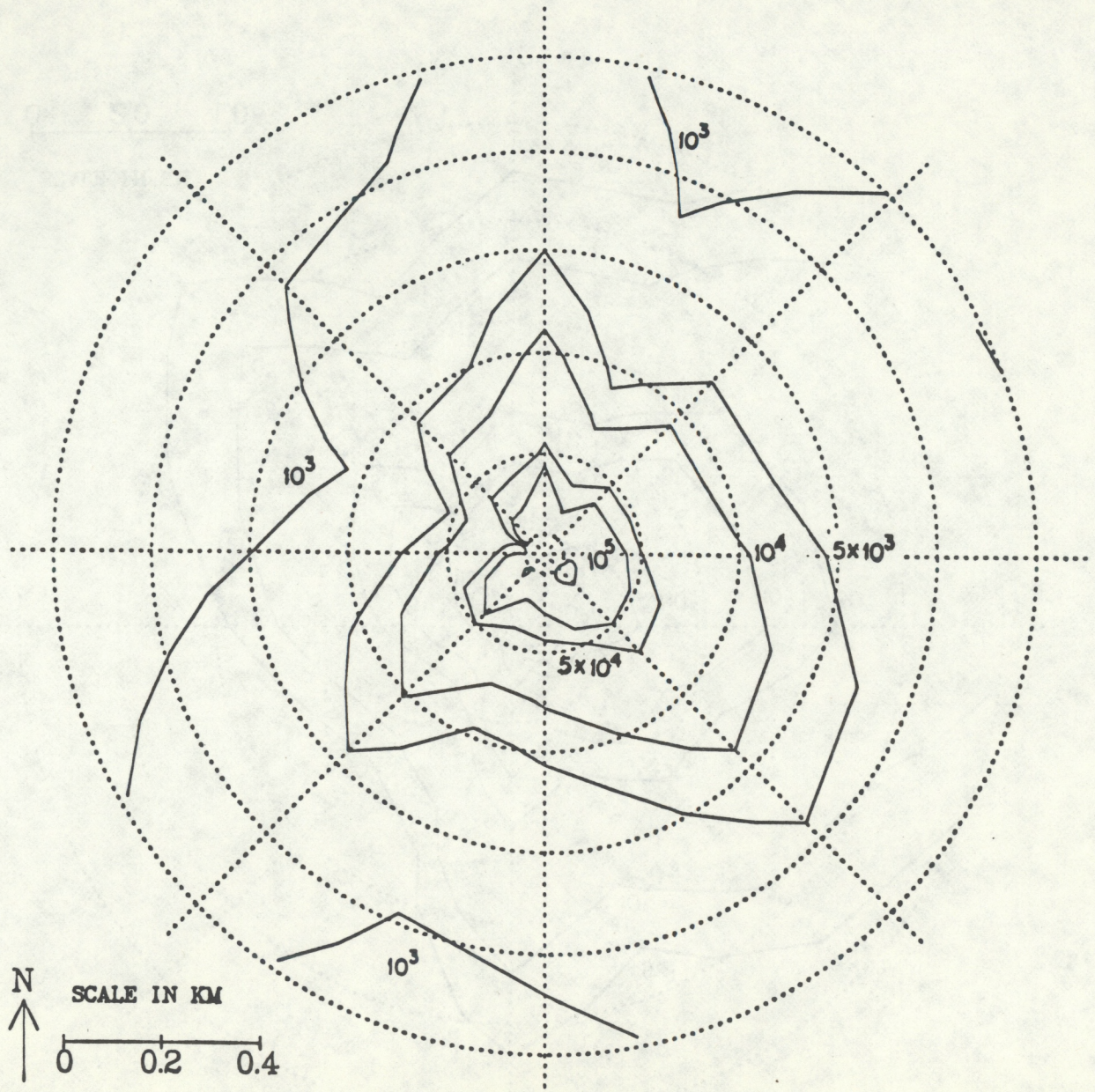

Figure 11. Isopleths of sector-average monthly surface deposition flux ($kg/km^2/month$) in the near-field region for the month of April (Case I).

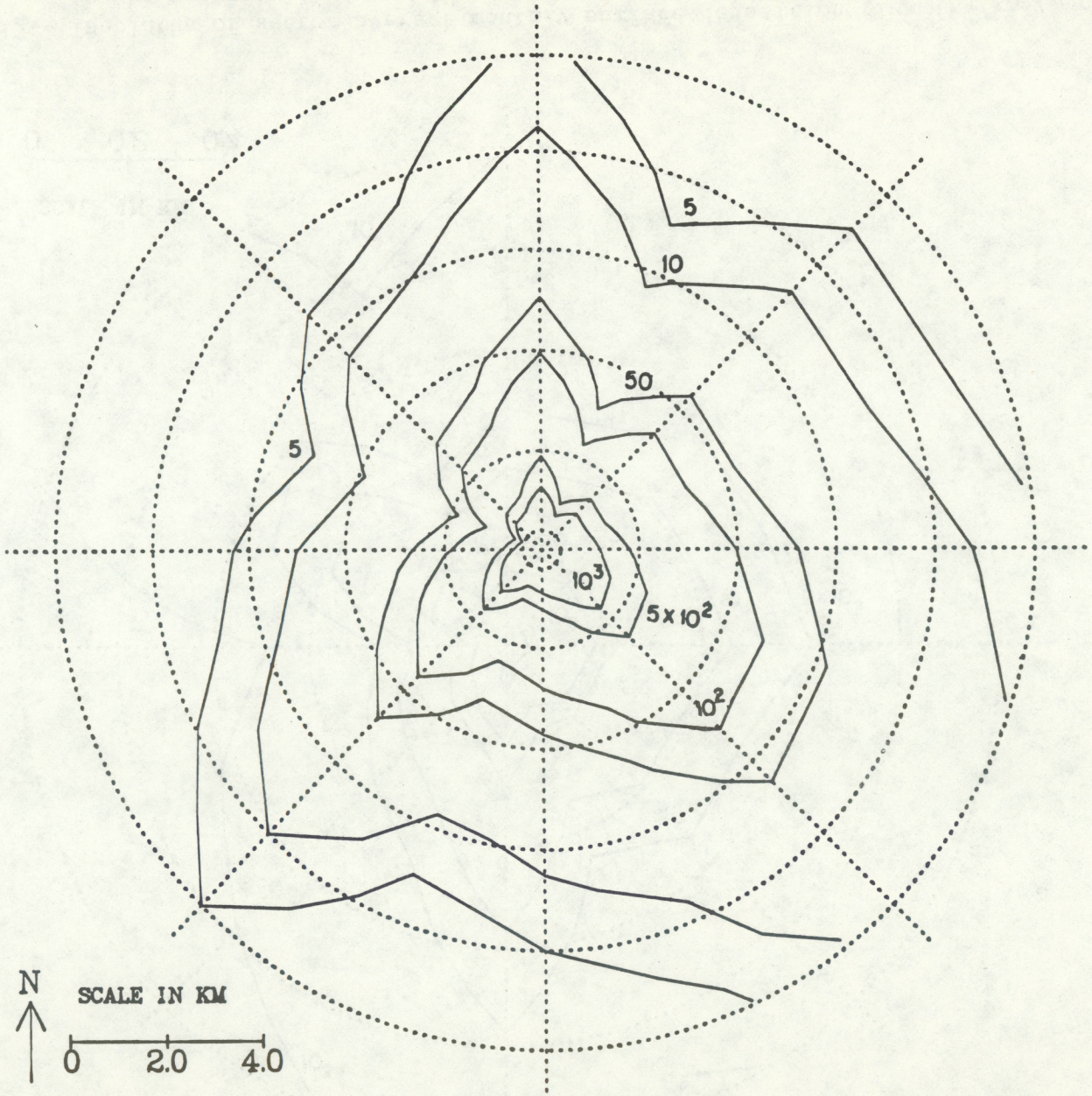

Figure 12. Isopleths of sector-average monthly surface deposition flux ($kg/km^2/month$) in the far-field region for the month of April (Case I).

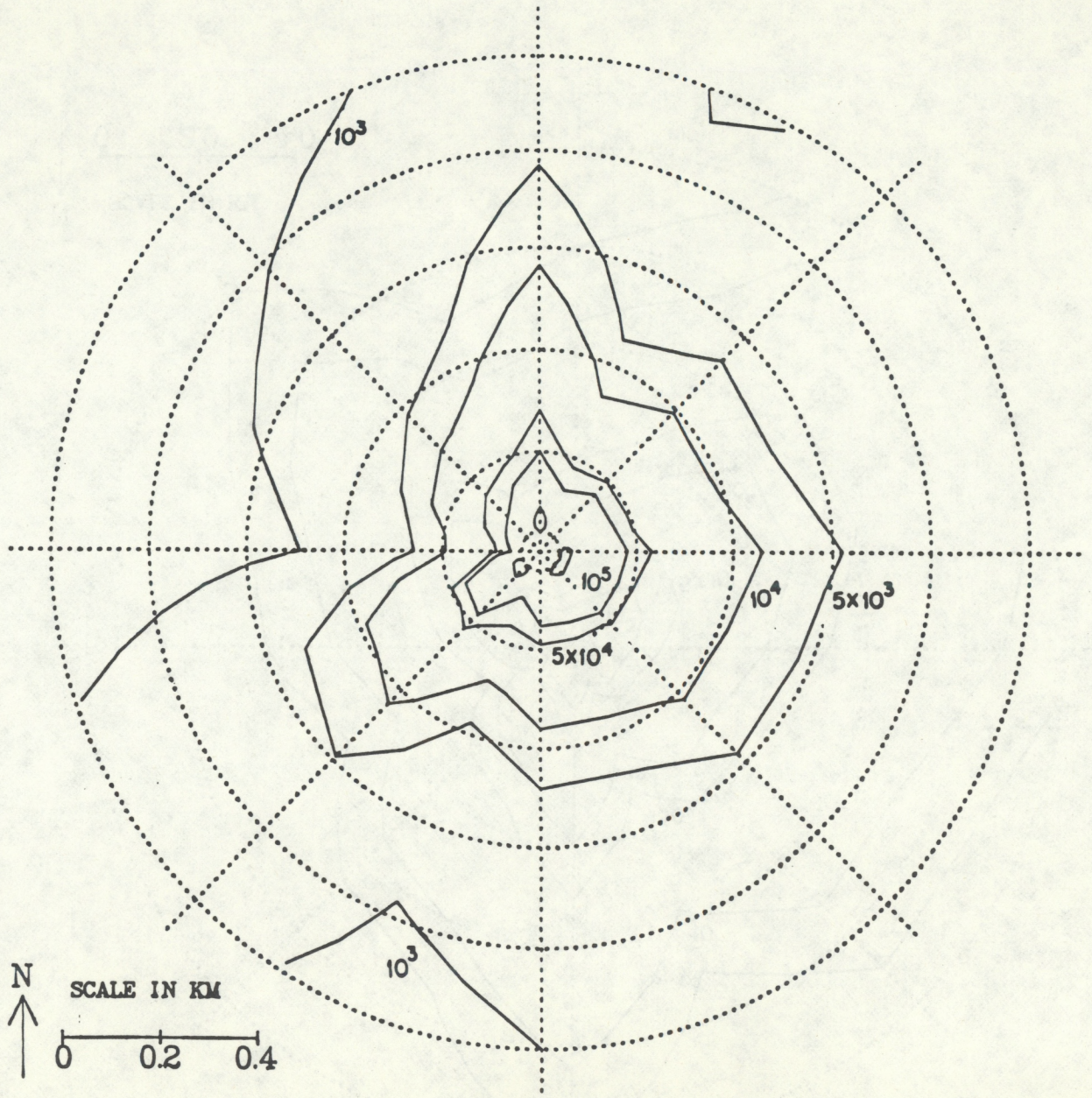

Figure 13. Isopleths of sector-average monthly surface deposition flux (kg/km^2/month) in the near-field region for the month of July (Case I).

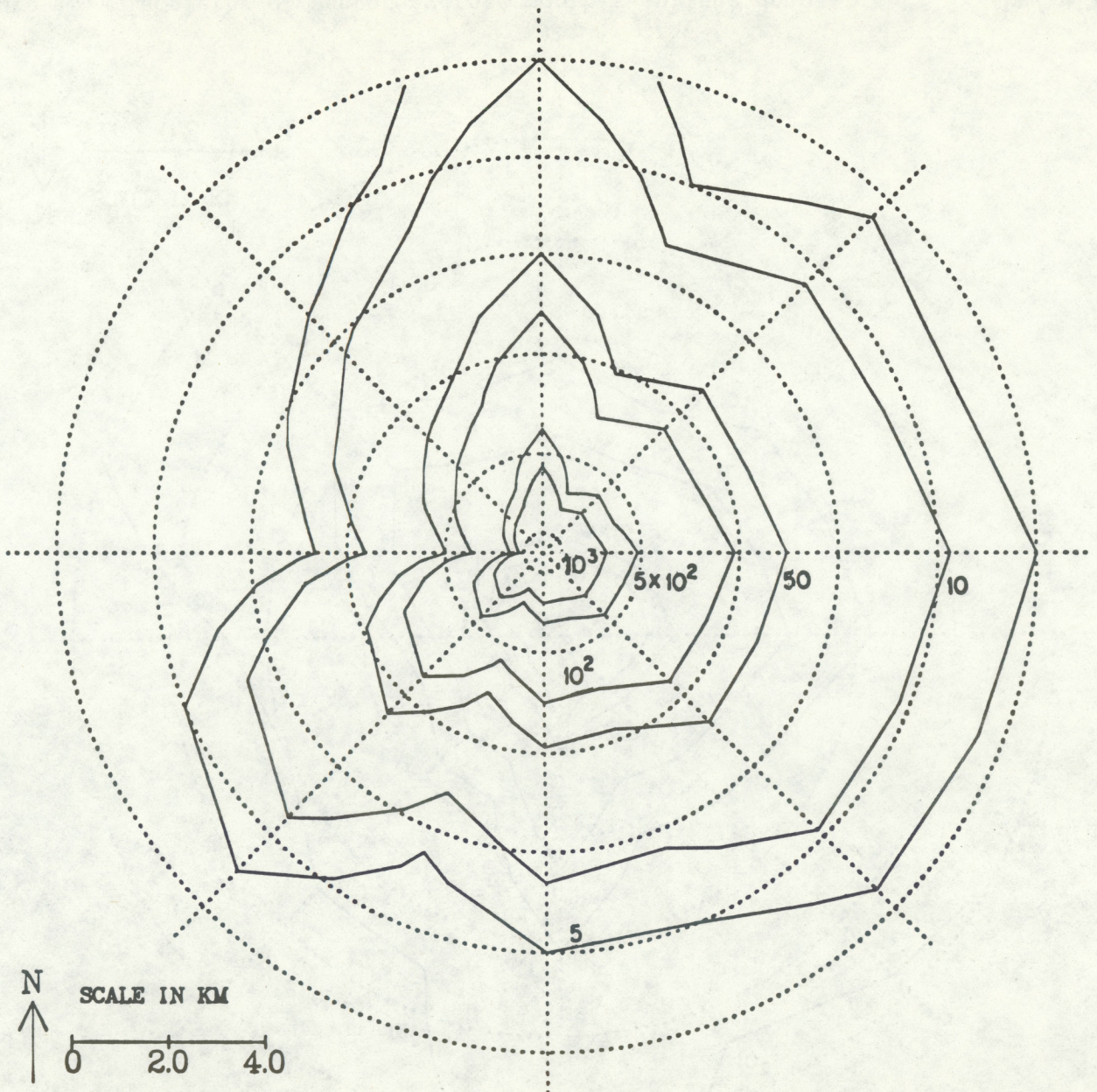

Figure 14. Isopleths of sector-average monthly surface deposition flux (kg/km^2/month) in the far-field region for the month of July (Case I).

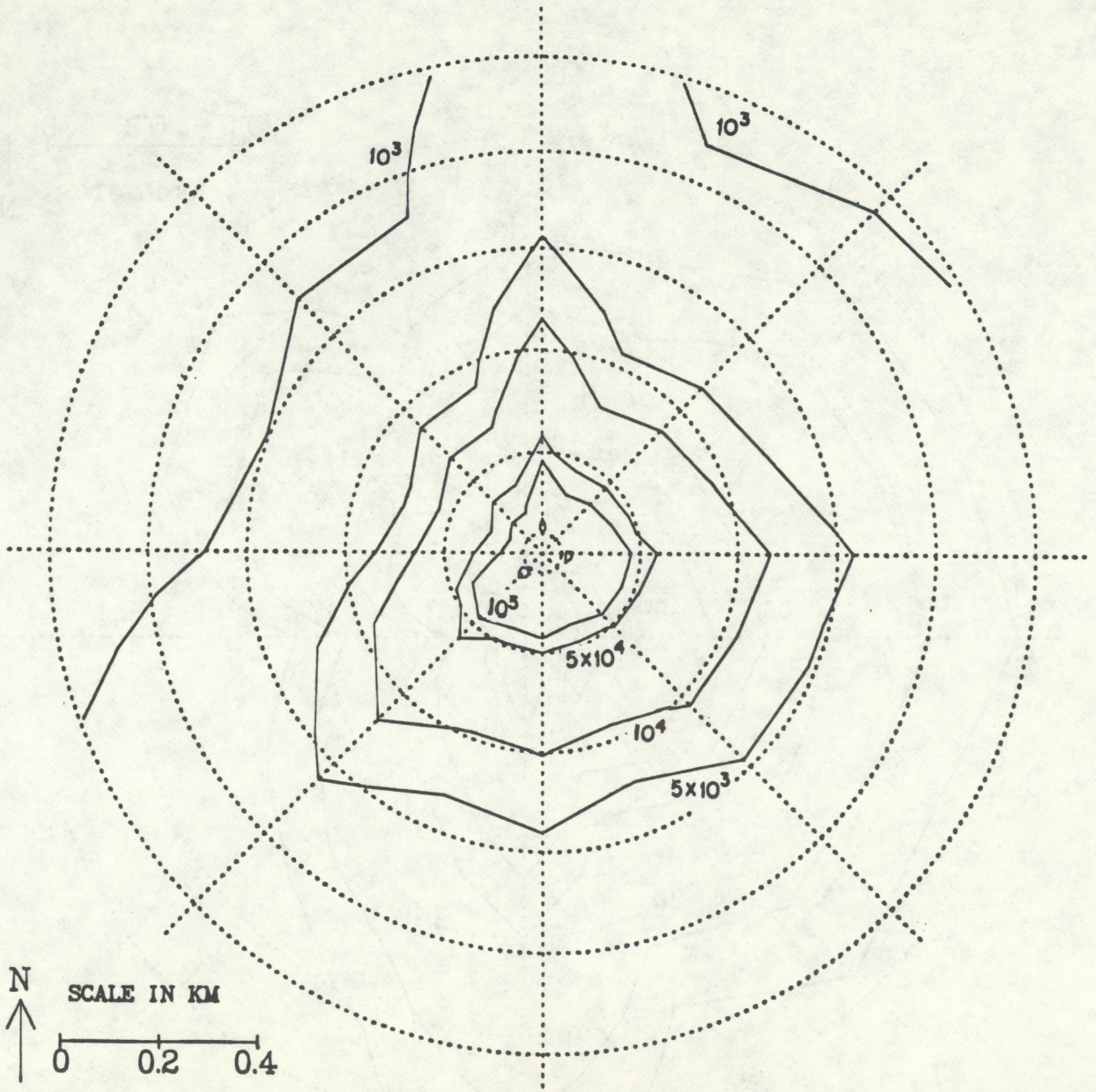

Figure 15. Isopleths of sector-average monthly surface deposition flux (kg/km^2/month) in the near-field region for the month of October (Case I).

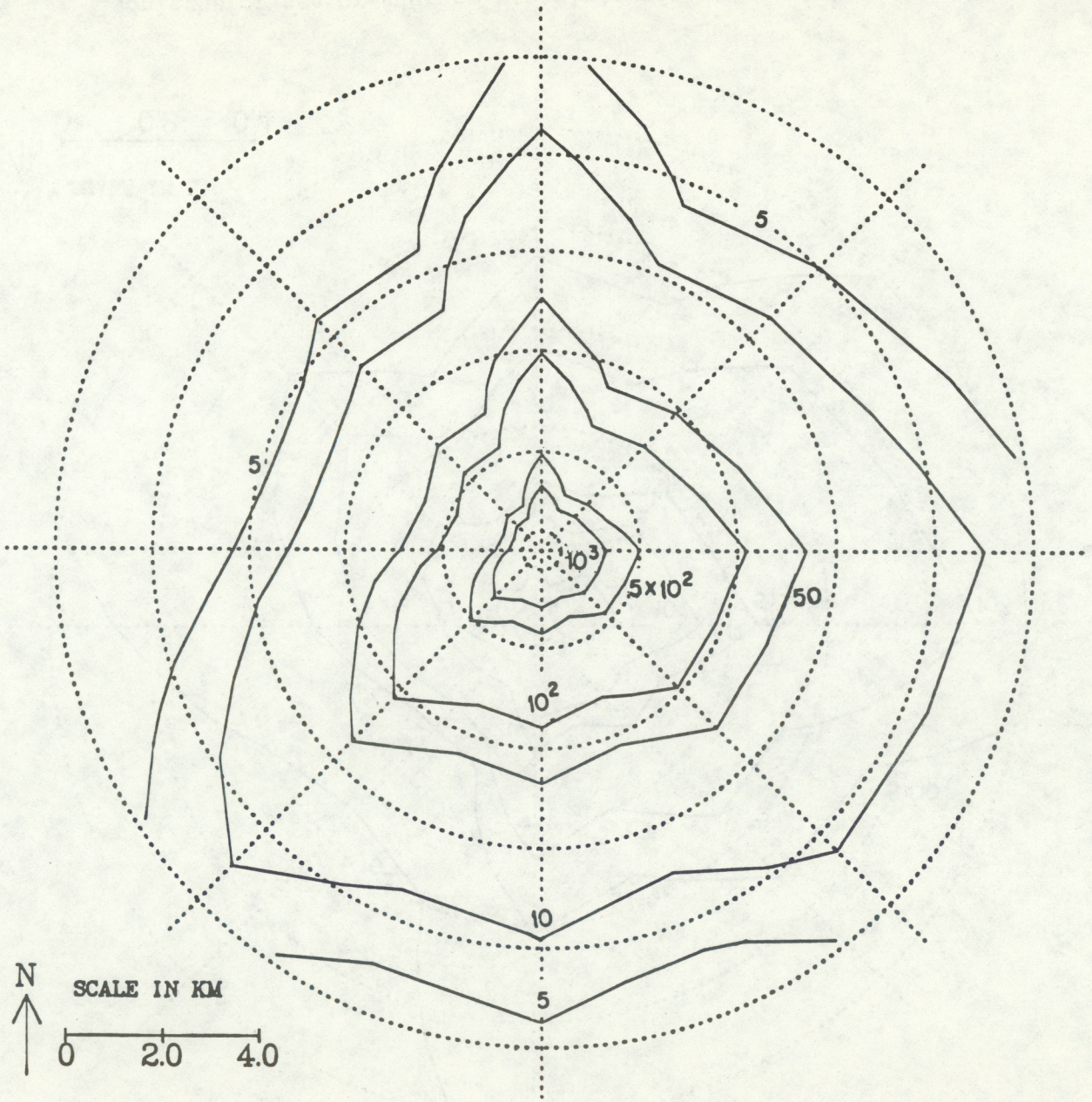

Figure 16. Isopleths of sector-average monthly surface deposition flux ($kg/km^2/month$) in the far-field region for the month of October (Case I).

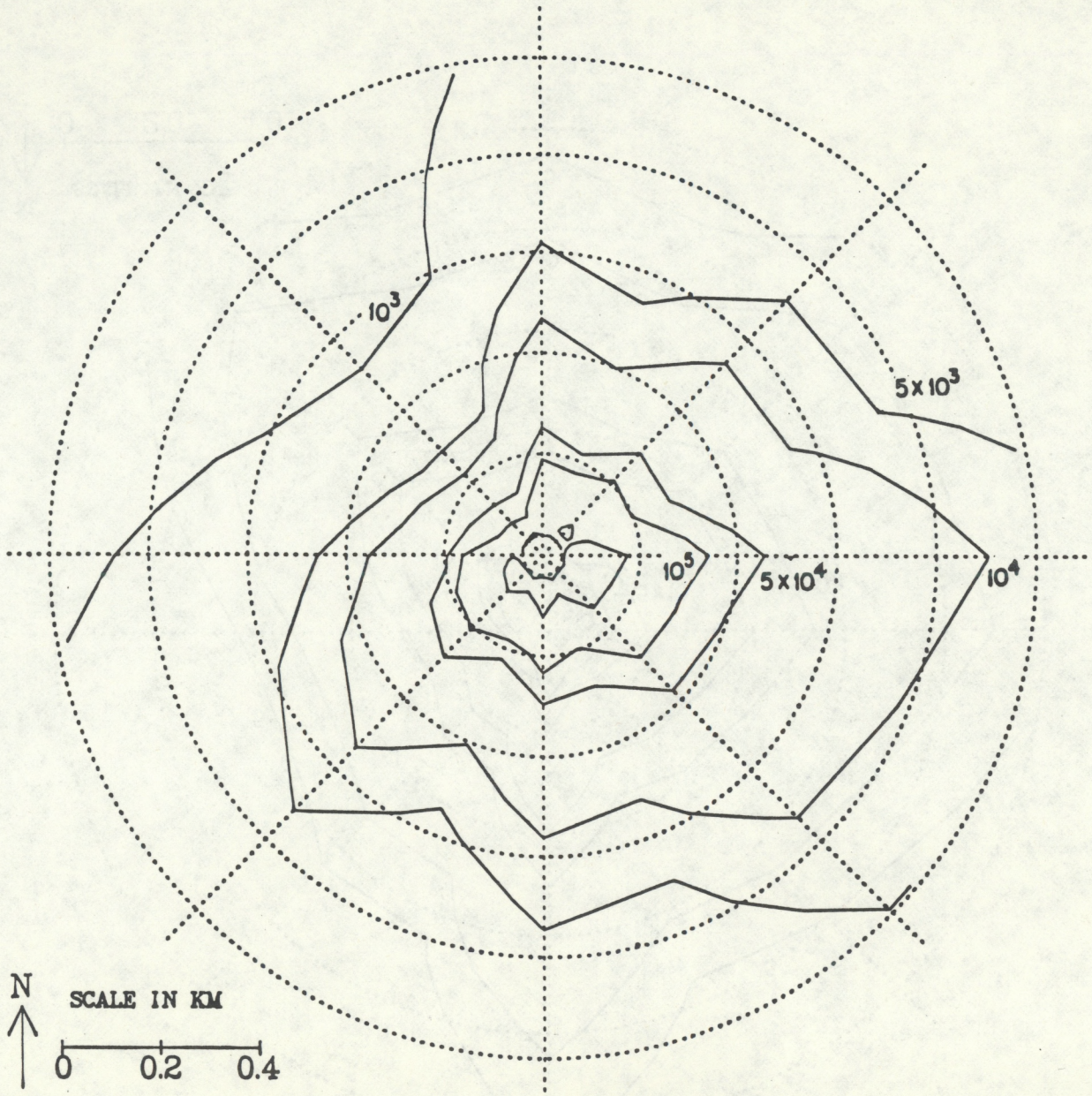

Figure 17. Isopleths of sector-average monthly surface deposition flux ($kg/km^2/month$) in the near-field region for the month of January (Case II).

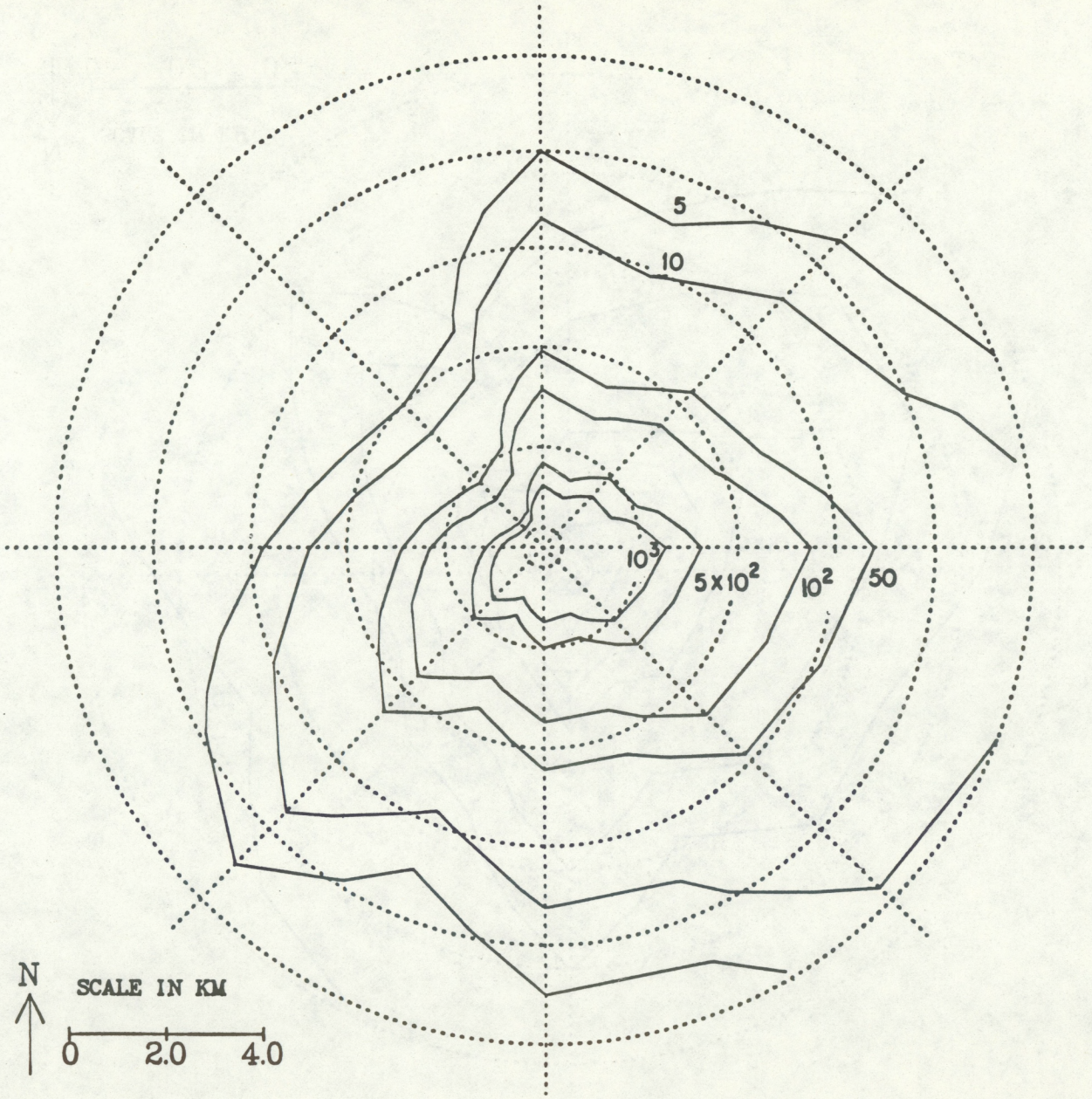

Figure 18. Isopleths of sector-average monthly surface deposition flux ($kg/km^2/month$) in the far-field region for the month of January (Case II).

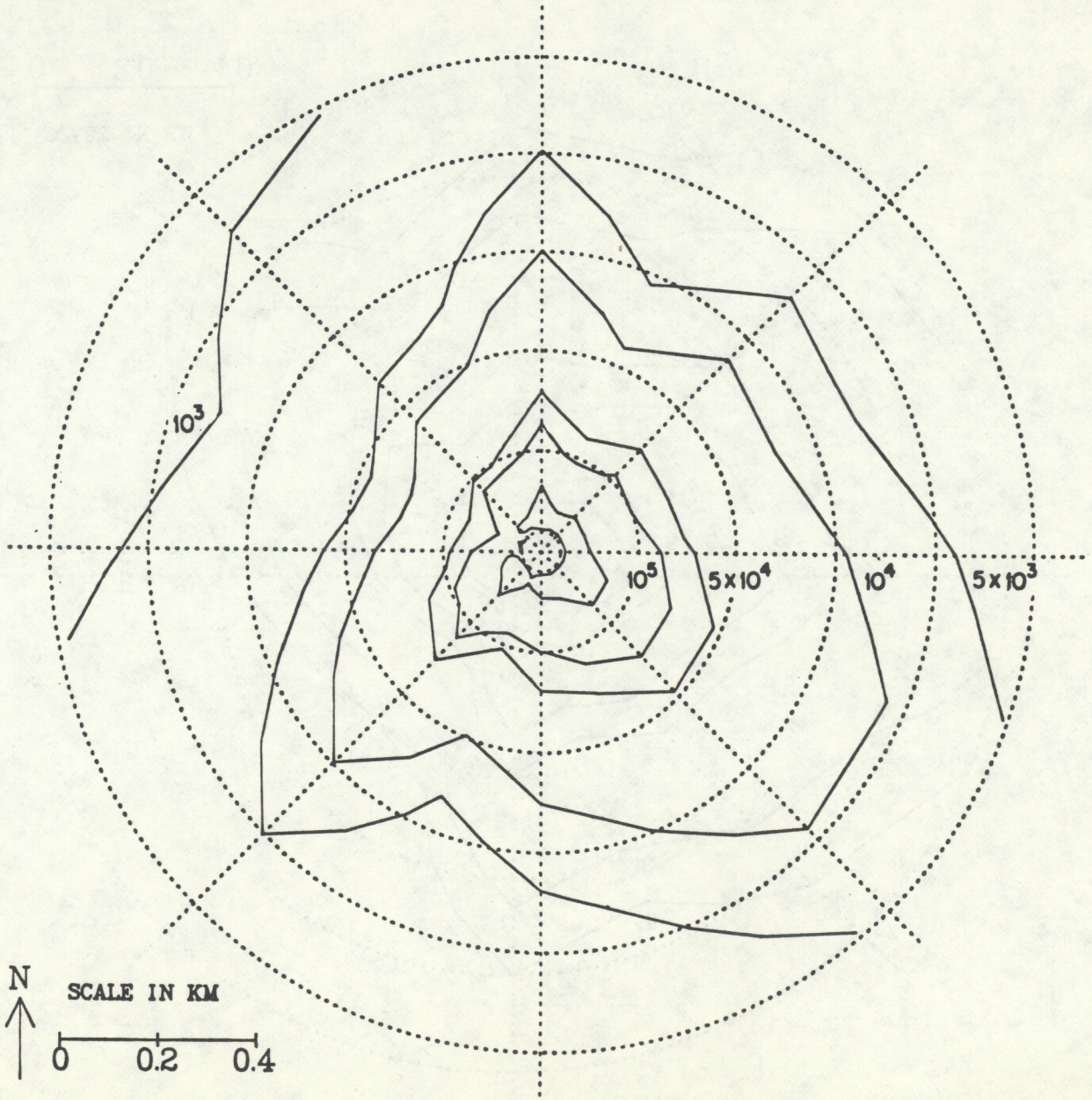

Figure 19. Isopleths of sector-average monthly surface deposition flux (kg/km^2/month) in the near-field region for the month of April (Case II).

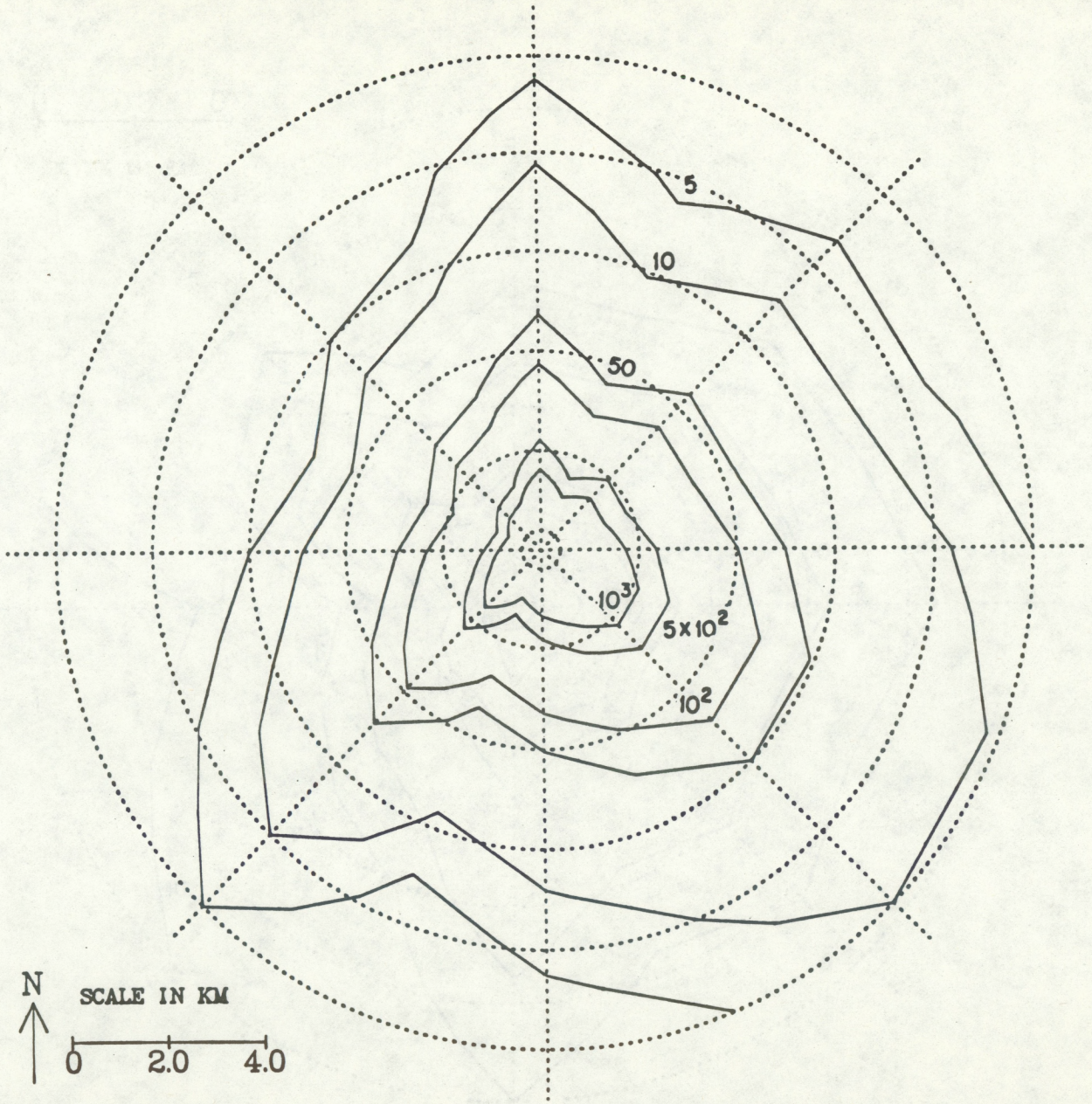

Figure 20. Isopleths of sector-average monthly surface deposition flux ($kg/km^2/month$) in the far-field region for the month of April (Case II).

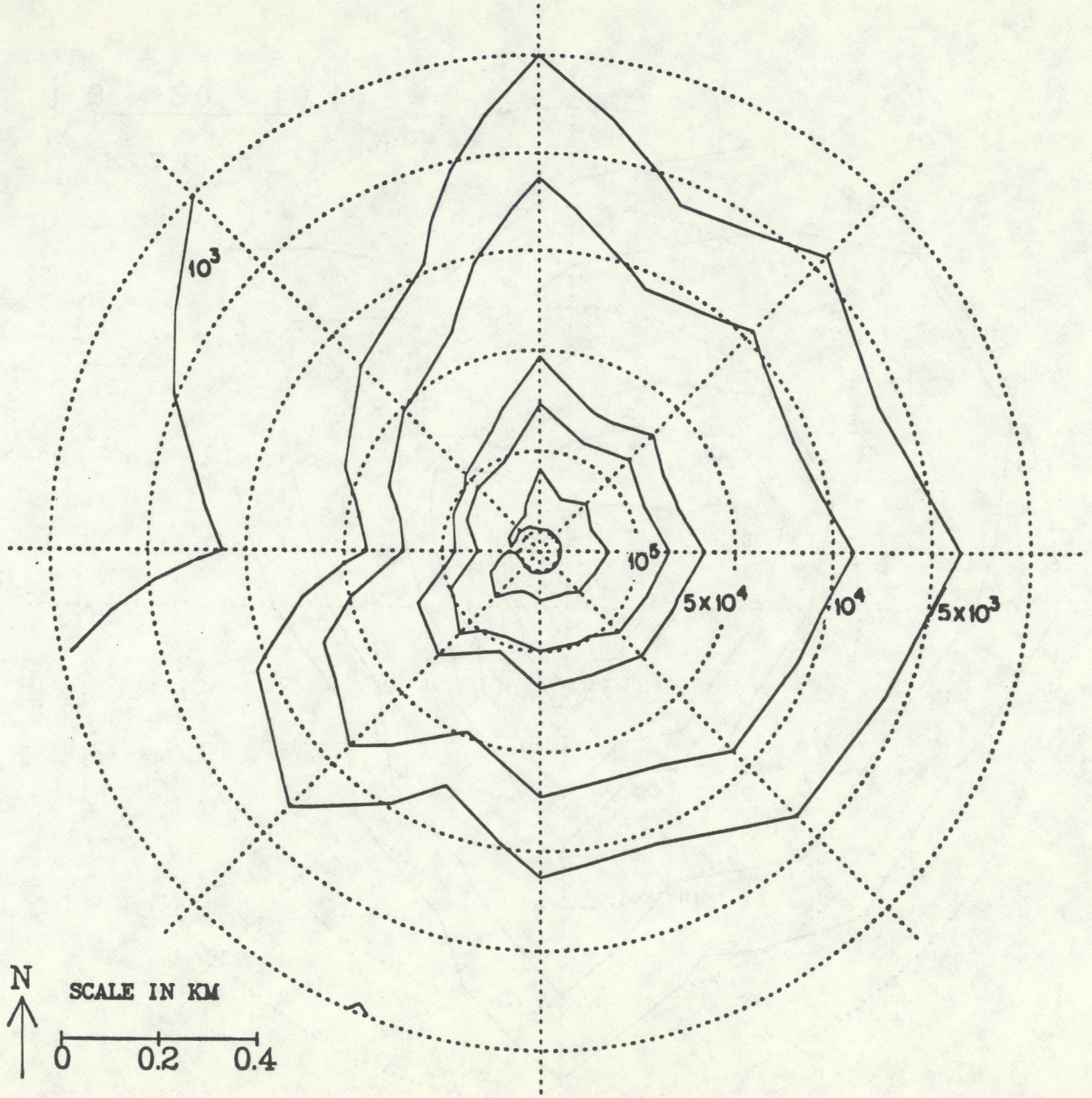

Figure 21. Isopleths of sector-average monthly surface deposition flux (kg/km^2/month) in the near-field region for the month of July (Case II).

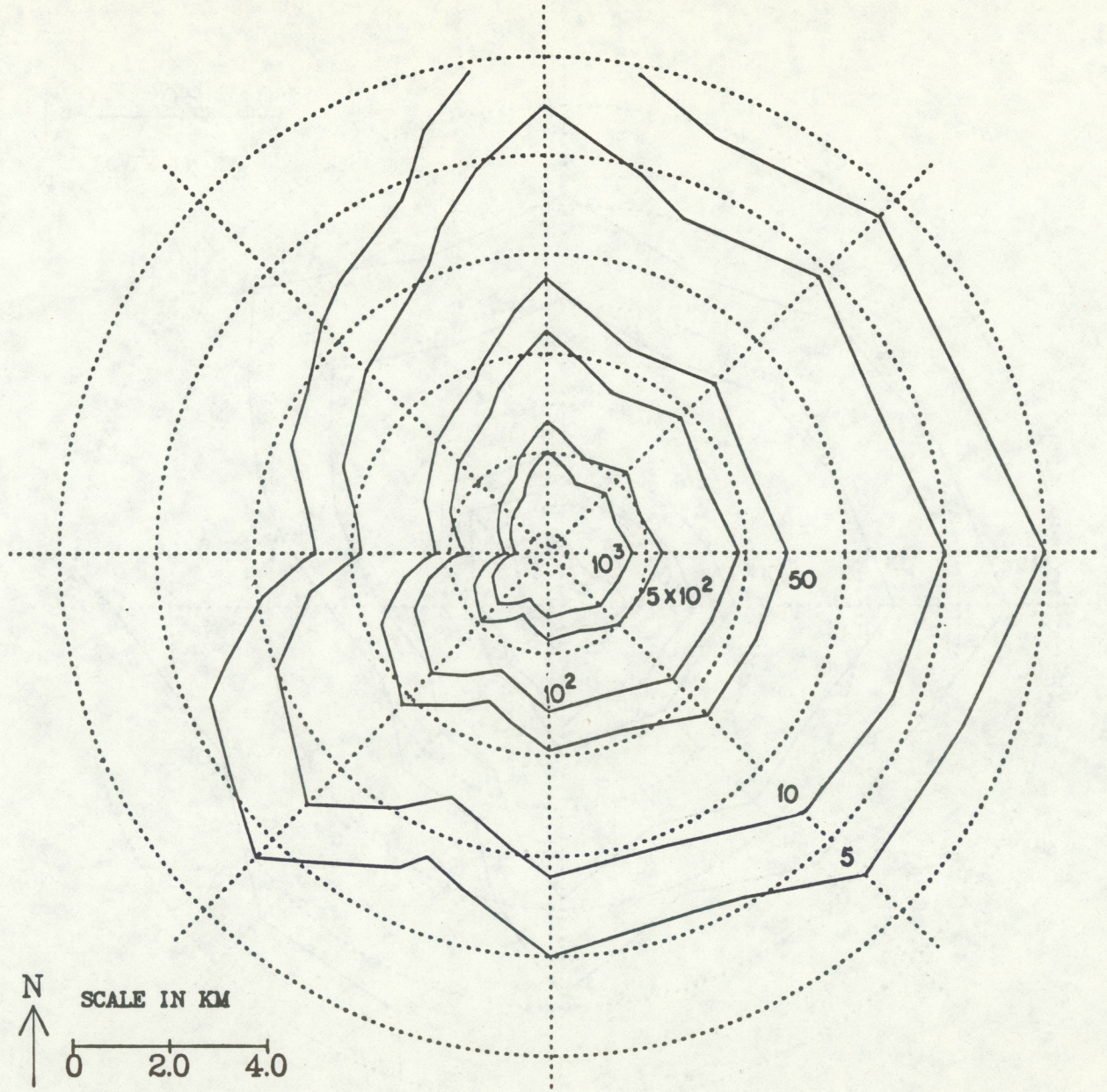

Figure 22. Isopleths of sector-average monthly surface deposition flux (kg/km^2/month) in the far-field region for the month of July (Case II).

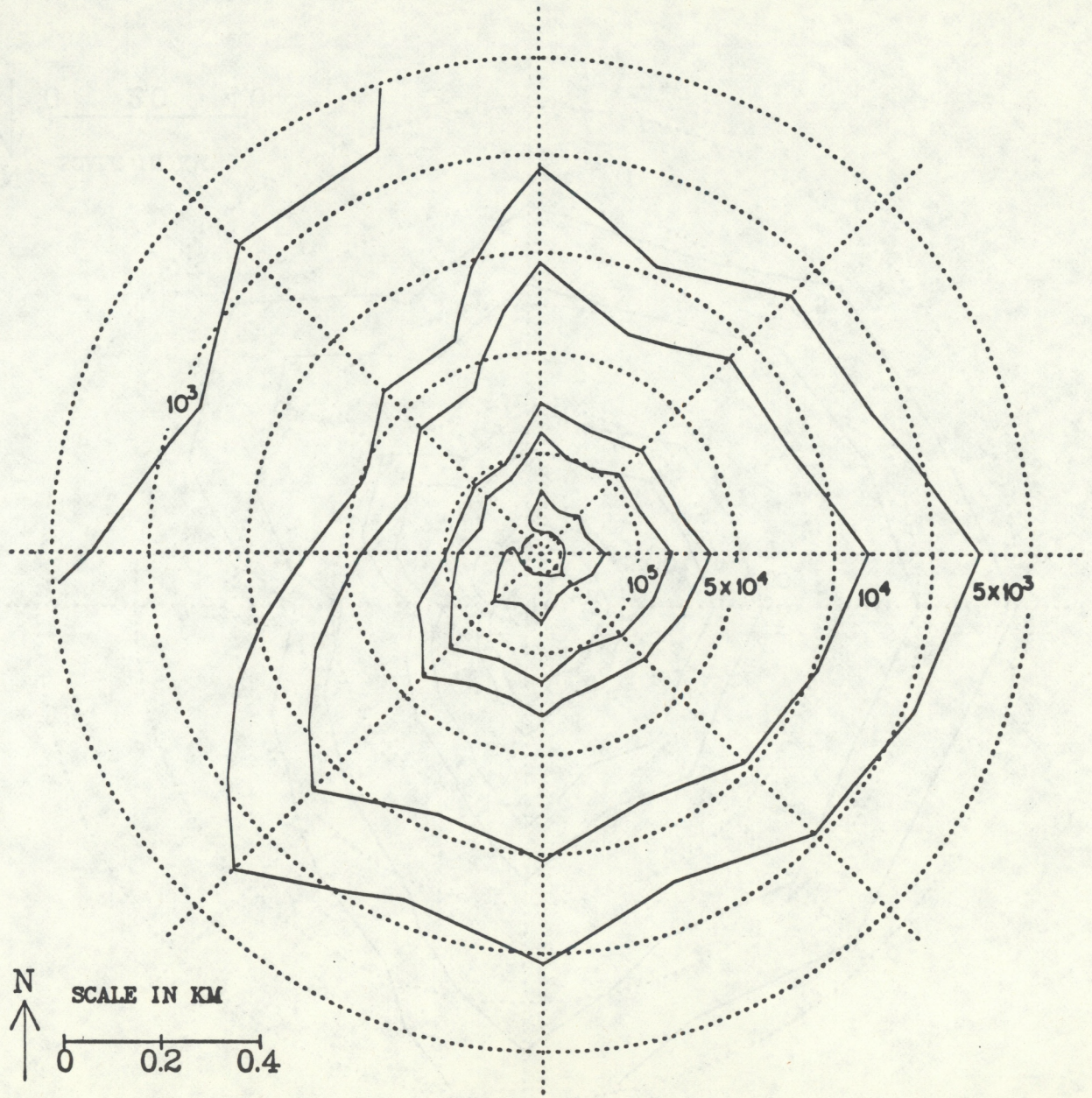

Figure 23. Isopleths of sector-average monthly surface deposition flux (kg/km^2/month) in the near-field region for the month of October (Case II).

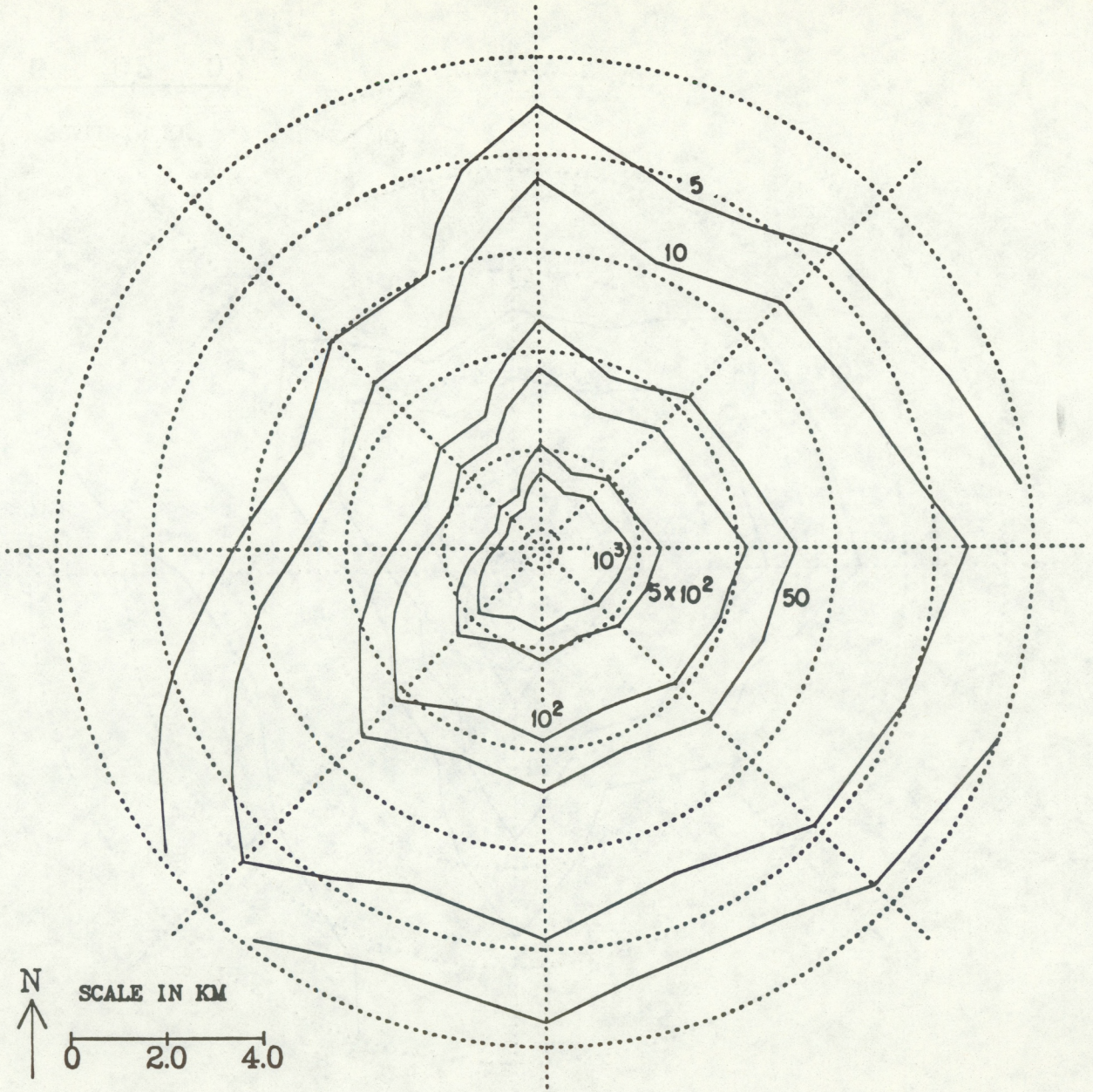

Figure 24. Isopleths of sector-average monthly surface deposition flux (kg/km^2/month) in the far-field region for the month of October (Case II).

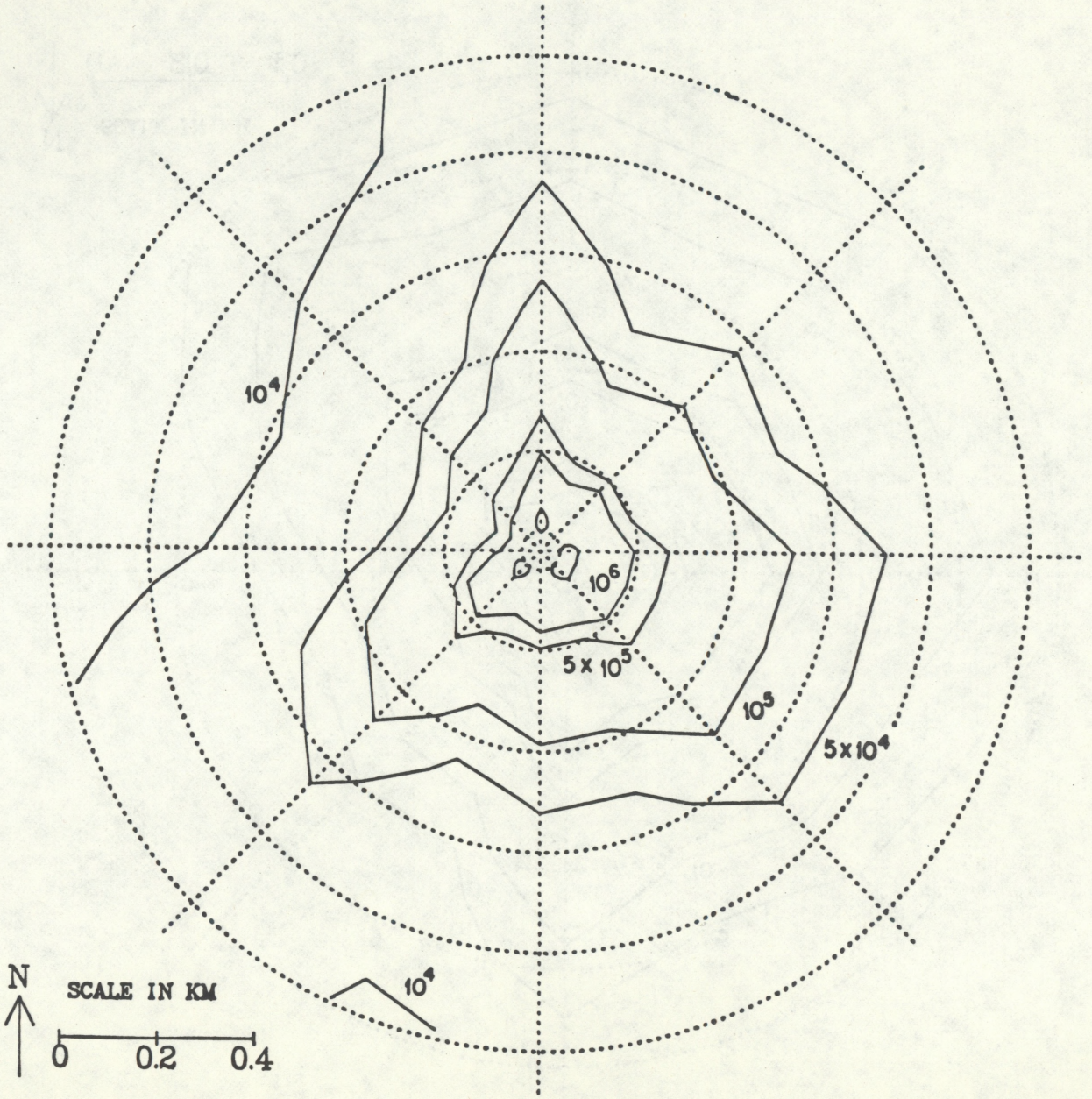

Figure 25. Isopleths of sector-average yearly surface deposition flux (kg/km^2/year) in the near-field region (Case I).

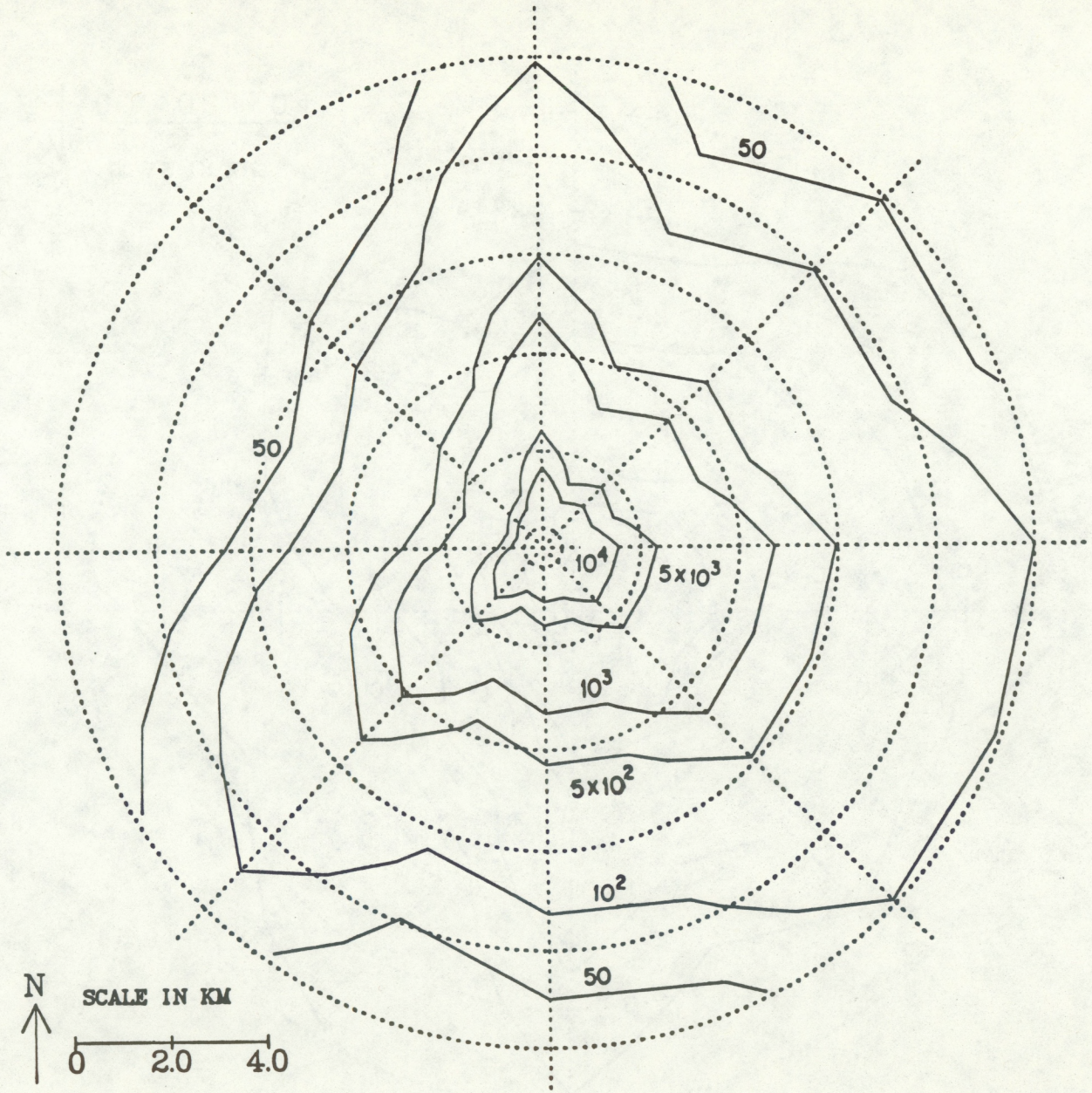

Figure 26. Isopleths of sector-average yearly surface deposition flux (kg/km^2/year) in the far-field region (Case I).

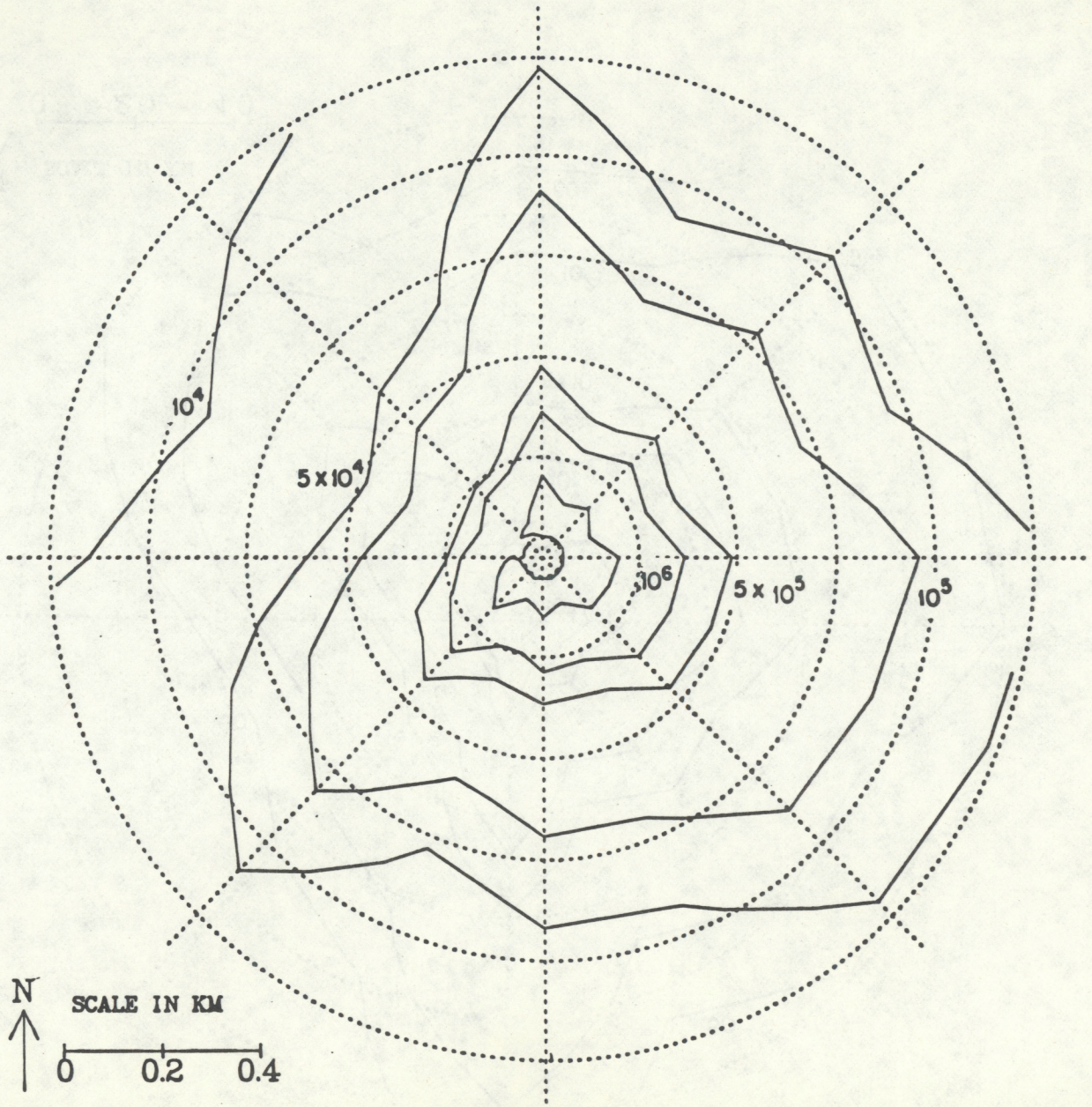

Figure 27. Isopleths of sector-average yearly surface deposition flux ($kg/km^2/year$) in the near-field region (Case II).

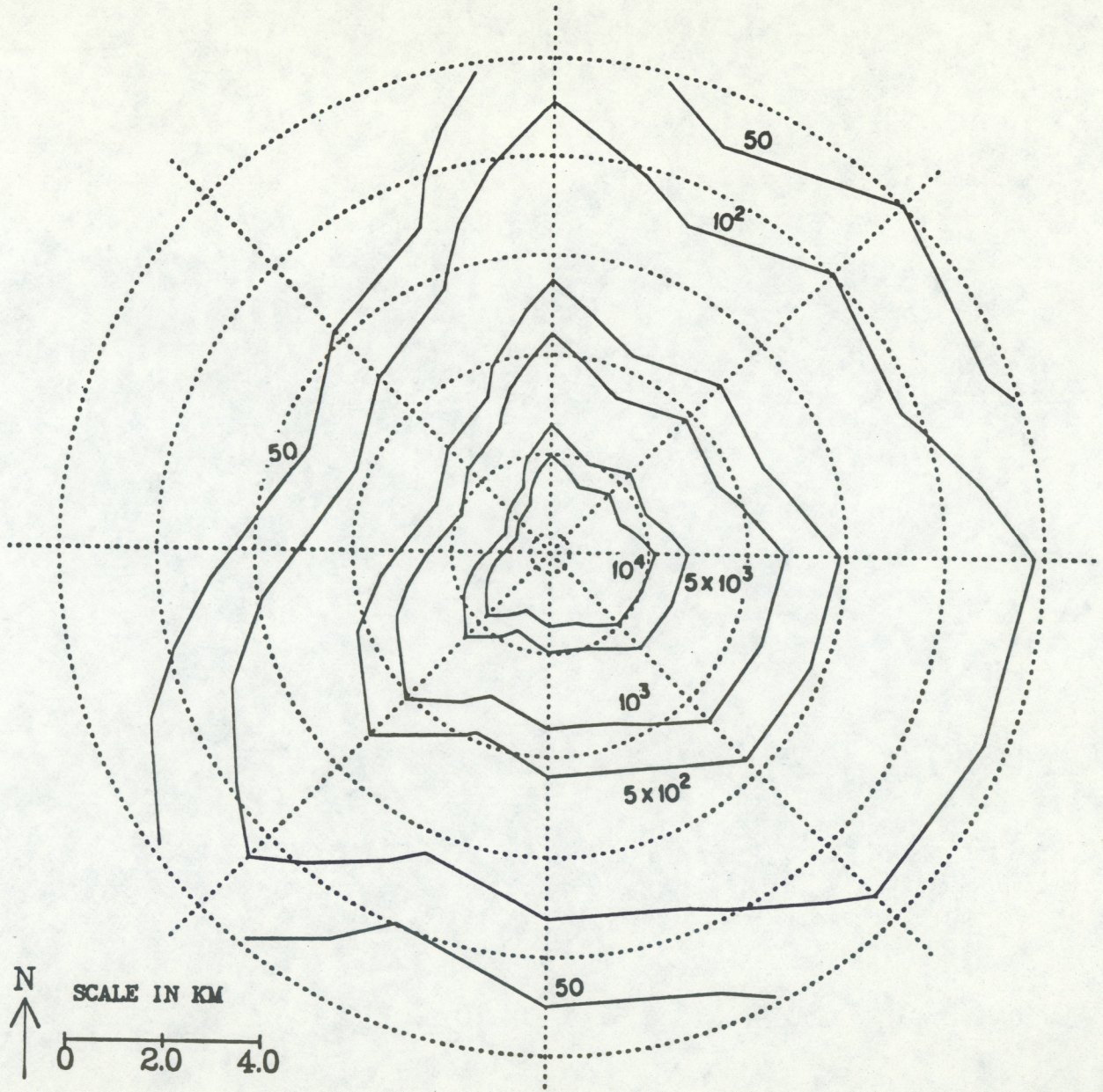

Figure 28. Isopleths of sector-average yearly surface deposition flux (kg/km^2/year) in the far-field region (Case II).